Chapter 6
Magnetospheric MHD Resonances and ULF Pulsations

Abstract This chapter deals with the low-frequency MHD oscillation of the whole magnetosphere and ULF pulsations including their origins and magnetospheric plasma instabilities. We discuss briefly magnetospheric models and the generation of field-line resonances (FLRs) and cavity modes. Properties of MHD waves propagating in the solar wind are covered. In the remainder of this chapter we examine source mechanisms of natural electromagnetic ULF noises.

Keywords Cavity mode • Field-line resonances (FLRs) • Plasma instabilities • Space weather • ULF electromagnetic noises

6.1 Structure of Global Magnetospheric Oscillations

6.1.1 An Axisymmetric Magnetosphere Model

It is customary to believe that the MHD oscillation of the whole magnetosphere was originally studied by Dungey (1954) who derived equations for the eigen oscillation of an axisymmetric magnetosphere. The normal magnetospheric MHD oscillation, which is independent of azimuthal angle φ, can be split into two practically uncoupled modes: toroidal and poloidal modes depending on their polarization. In the poloidal modes, the electric field oscillates in the azimuthal direction, while the magnetic field and plasma velocity pulsate across magnetic shells. By contrast, in the case of the toroidal modes, the electric field is in the meridional plane, while the magnetic field and plasma velocity oscillate in the azimuthal direction. These types of the magnetospheric MHD oscillation have been studied intensively for several decades and much is now known of their properties (Radoski 1967a,b; Radoski and Carovillano 1969; Cummings et al. 1969; Krylov and Lifshitz 1984).

V. Surkov and M. Hayakawa, *Ultra and Extremely Low Frequency Electromagnetic Fields*, Springer Geophysics, DOI 10.1007/978-4-431-54367-1_6,

The neutral gas is so rarefied at magnetospheric heights that the number density of ions is much greater than that of neutrals, so that the plasma can be considered fully ionized in this region. Furthermore, the plasma itself is so tenuous that $\nu_{ei} \ll \Omega_i$ and thus the medium can be treated as a collisionless magnetized plasma. In such a case we can use the MHD approach, in which, as we have noted in Sect. 1.2.2, the plasma is considered as a single fluid having infinite conductivity. This means that in a reference frame moving at plasma velocity $\mathbf{V}$ the electrical field $\mathbf{E}' = \mathbf{E} + \mathbf{V} \times \mathbf{B}$ vanishes in both directions parallel and perpendicular to $\mathbf{B}$, whence it follows that in a reference frame fixed to the Earth $\mathbf{E} = \mathbf{B} \times \mathbf{V}$.

The magnetospheric plasma dynamics is described by Eq. (1.13), which relates the plasma velocity to the forces acting on the plasma. This equation in its general form contains the pressure gradient, the terms describing the gravitational and "viscous" forces, and the magnetic/Ampere's force given by $\mathbf{j} \times \mathbf{B}$. In the reference frame fixed to the Earth this equation includes all the inertial forces acting on the plasma due to the Earth spin. The pressure gradient and the magnetic force dominate if the typical frequencies are smaller than 0.1 Hz. In this frequency range the gravity, viscosity, and inertial terms in Eq. (1.13) can be neglected.

Following Dungey (1954, 1963) we first assume that the geomagnetic field and electric currents in the magnetosphere are large enough so that the magnetic force in Eq. (1.13) is much greater than the pressure gradient. It should be noted that the plasma motion parallel to the magnetic field lines must be due to only the pressure gradient ∇P since the magnetic force $\mathbf{j} \times \mathbf{B}$ is always perpendicular to $\mathbf{B}$. On the other hand the plasma motion parallel to $\mathbf{B}$ does not greatly affect the magnetic field. In this picture the cancel of ∇P in Eq. (1.13) is not so a burdensome condition. Finally, we have

$$\rho d\mathbf{V}/dt = \mathbf{j} \times \mathbf{B}, \tag{6.1}$$

where ρ is the plasma mass density, and the total time-derivative d/dt is given by Eq. (1.12). To treat the plasma dynamics, Maxwell's equations are required, whose full forms are given by Eqs. (1.1)–(1.4). Since the vacuum displacement current $\partial_t \mathbf{D}$ can be ignored due to the high plasma conductivity, Eq. (1.1) is simplified to the form in which the curl of magnetic field is related to the conduction current $\mathbf{j}$ through Eq. (1.5).

Substituting $\mathbf{E} = \mathbf{B} \times \mathbf{V}$ into Eq. (1.2) gives Eq. (1.18). The meaning of this equation is that the magnetic field is frozen to the conducting plasma and thus can be considered to move with the plasma. The concept of "frozen-in" magnetic field lines has been discussed in more detail in Sect. 1.2.1.

Let $\delta\mathbf{B}$ be the small perturbation of the ambient/geomagnetic field $\mathbf{B}_0$, so that $\mathbf{B} = \mathbf{B}_0 + \delta\mathbf{B}$, and $|\delta\mathbf{B}| \ll |\mathbf{B}_0|$. The unperturbed geomagnetic field $\mathbf{B}_0$ is not a function of time. In the first approximation, one can replace the term $\mathbf{V} \times \mathbf{B}$ in Eq. (1.18) with $\mathbf{V} \times \mathbf{B}_0$. After these simplifications we come to the following equation:

$$\partial_t \delta\mathbf{B} = \nabla \times (\mathbf{V} \times \mathbf{B}_0)\,. \tag{6.2}$$

The same approximations can be applied to Eq. (1.35) to yield

$$\mathbf{E} = \mathbf{B}_0 \times \mathbf{V}. \tag{6.3}$$

Here $\mathbf{E}$ denotes the perturbation of the electric field since a constant electric field is assumed to be absent. Returning to the equation of motion (6.1) and substituting Eq. (1.5) for $\mathbf{j}$ into this equation, we have

$$\mu_0 \rho d\mathbf{V}/dt = (\nabla \times \mathbf{B}) \times \mathbf{B}. \tag{6.4}$$

In what follows we restrict our analysis to the case of a dipole approximation of the geomagnetic field $\mathbf{B}_0$, given by Eq. (1.30). Substituting $\mathbf{B} = \mathbf{B}_0 + \delta\mathbf{B}$ into Eq. (6.4), taking into account that $\nabla \times \mathbf{B}_0 = 0$, and considering the small amplitude waves, so that $d\mathbf{V}/dt \approx \partial_t \mathbf{V}$, the equation of plasma motion is reduced to

$$\mu_0 \rho \partial_t \mathbf{V} = (\nabla \times \delta\mathbf{B}) \times \mathbf{B}_0. \tag{6.5}$$

Taking the cross product of both sides of Eq. (6.5) with $\mathbf{B}_0$ and substituting Eq. (6.3) for $\mathbf{B}_0 \times \mathbf{V}$ into this equation yields

$$\mu_0 \rho \partial_t \mathbf{E} = \mathbf{B}_0 \times [(\nabla \times \delta\mathbf{B}) \times \mathbf{B}_0]. \tag{6.6}$$

Now we should use Eq. (1.55) for triple cross product with $\mathbf{A}_1 = \mathbf{A}_3 = \mathbf{B}_0$ and $\mathbf{A}_2 = \delta\mathbf{B}$. Applying this equation to the right-hand side of Eq. (6.6) yields

$$\mu_0 \rho \partial_t \mathbf{E} = B_0^2 (\nabla \times \delta\mathbf{B}) - \mathbf{B}_0 [\mathbf{B}_0 \cdot (\nabla \times \delta\mathbf{B})]. \tag{6.7}$$

The set of Eqs. (6.2), (6.3), and (6.7) constitutes the suitable single-fluid description of dynamics of a magnetized plasma. A general analytical solution of the plasma dynamics problem is not yet at hand although the numerical solutions, which can be applied to the actual magnetosphere, have been studied in detail (e.g., see Lee and Lysak 1989, 1990; Alperovich and Fedorov 2007).

As we have noted above, to the first order the Earth magnetic field is described through the dipole approximation. If the polar z axis is positive parallel to the Earth's magnetic moment $\mathbf{M}_e$ and the origin of the coordinate system is in the Earth center, then the Earth's dipole magnetic field is the axially symmetrical one and has only the components B_r and B_θ given by Eq. (1.33) while $B_\varphi = 0$.

In this approximation we consider the axially symmetrical problem, in which all the values are independent on φ. As we shall see, in this case the equation set is split into two independent parts: the first one contains the components of electromagnetic perturbations δB_φ, E_r, E_θ and azimuthal velocity V_φ, and the second one contains the components δB_r, δB_θ, E_φ, V_r, and V_θ. The first mode is referred to as the shear Alfvén wave and the next one is the FMS/compressional wave. According to geophysical terminology, the standing quasi-Alfvén wave which contains the azimuthal magnetic field δB_φ is termed the toroidal mode, while the standing compressional wave ($\delta B_r, \delta B_\theta$) is referred to as the poloidal mode.

So, the polarization of the Alfvén oscillations differs from that of the poloidal mode. The electric field of the poloidal mode has only an azimuthal component, while the magnetic field perturbations and plasma velocity are directed across the magnetic shell.

6.1.2 Toroidal Mode

The shear Alfvén mode could have an important role to play in the generation of field line resonances (FLRs hereafter). These kinds of standing waves in the magnetosphere have frequently been observed onboard the satellites (e.g., see Glassmeier 1995) so that a spatial structure and the source mechanisms of these waves are of a special interest in geophysical studies.

Using the spherical coordinates, the azimuthal components of Eq. (6.2) can be written as

$$\partial_t \delta B_\varphi = r^{-1} \left\{ \partial_r \left[r \left(\mathbf{V} \times \mathbf{B}_0 \right)_\theta \right] - \partial_\theta \left[\left(\mathbf{V} \times \mathbf{B}_0 \right)_r \right] \right\}. \tag{6.8}$$

Substituting the angular and radial components of $\mathbf{V} \times \mathbf{B}_0$ into Eq. (6.8) yields

$$\partial_t \delta B_\varphi = r^{-1} \left\{ \partial_r \left(r V_\varphi B_r \right) - \partial_\theta \left(V_\varphi B_\theta \right) \right\}. \tag{6.9}$$

The components B_r and B_θ of undisturbed Earth's magnetic field are given by Eq. (1.33). Substituting these components into Eq. (6.9) and rearranging this equation yields

$$\partial_t \delta B_\varphi = r \sin\theta \left(\mathbf{B}_0 \cdot \nabla \right) \left(\frac{V_\varphi}{r \sin\theta} \right), \tag{6.10}$$

where we have introduced the differential operator acting on the functions of variables r and θ:

$$\mathbf{B}_0 \cdot \nabla = \frac{\mu_0 M_e}{4\pi r^3} \left(2\cos\theta \partial_r + \frac{\sin\theta}{r} \partial_\theta \right). \tag{6.11}$$

Here M_e denotes the Earth's magnetic dipole moment.

The azimuthal component of the equation of motion (6.5) has the form

$$\rho \partial_t V_\varphi = \frac{M_e}{4\pi r^4} \left\{ \partial_\theta \left(\delta B_\varphi \sin\theta \right) + 2\cos\theta \partial_r \left(r \delta B_\varphi \right) \right\}. \tag{6.12}$$

Combining this equation with Eq. (1.33) for the components B_r and B_θ and rearranging, we find that

$$\mu_0 \rho r \sin\theta \partial_t V_\varphi = \left(\mathbf{B}_0 \cdot \nabla \right) \left(r \sin\theta \delta B_\varphi \right). \tag{6.13}$$

The electric field components can be found from Eq. (6.3)

$$E_r = B_\theta V_\varphi, \quad E_\theta = -B_r V_\varphi. \tag{6.14}$$

It is interesting to note that the scalar product of the electric field (6.14) with the vector $\mathbf{B}_0 = (B_r, B_\theta, 0)$ equals zero, that is, the vector $\mathbf{E}$ is perpendicular to the Earth's dipole magnetic field $\mathbf{B}_0$. This implies that the electric field of the toroidal mode is perpendicular to the Earth magnetic field shells.

Considering the toroidal mode, we are thus left with the set of Eqs. (6.10), (6.13), and (6.14) for the functions δB_φ, V_φ, E_r, and E_θ. To study the standing waves, in effect finding the normal modes of the axisymmetric magnetosphere, all perturbed quantities are considered to vary as $\exp(-i\omega t)$, where ω is the frequency. Replacing the time-derivatives ∂_t with the factor $-i\omega$ and eliminating δB_φ from Eqs. (6.10) and (6.13) yields

$$\mu_0 \rho r \omega^2 \sin\theta V_\varphi + (\mathbf{B}_0 \cdot \nabla)\left[r^2 \sin^2\theta\, (\mathbf{B}_0 \cdot \nabla)\left(\frac{V_\varphi}{r\sin\theta}\right)\right] = 0. \tag{6.15}$$

The only differential operator occurred at this equation is the operator $(\mathbf{B}_0 \cdot \nabla)$, which defines in fact the directional derivative. In other words, this equation contains only derivative along the magnetic field lines. This means that Eq. (6.15) describes oscillations of the azimuthal velocity V_φ and magnetic shells that originate from the rotation of the field lines about the symmetry axis. Each magnetic shell can vibrate independently of each other. All the field lines belonging to the same magnetic shell must vibrate synchronously, that is, the magnetic shell vibrates as a whole. To study eigen oscillations of the shell, therefore, it is sufficient to consider the oscillations of one of the magnetic field lines.

Equation (6.15) should be supplemented by the proper boundary conditions at the ends of the magnetic field lines, that is at the points where the field lines intersect the high conducting ionospheric E layer and the Earth's surface. The skin-depth in the ionosphere at frequencies $f \lesssim 0.1$ Hz exceeds the thickness of the ionospheric conductive layer. In this notation, the E layer is usually treated in a "thin" ionosphere approximation, while the Earth can be considered as a perfect conductor, which reflects the electromagnetic waves totally. More usually we use the boundary conditions of the impedance type in which the electric and magnetic field components tangential to the ionosphere are related in a linear fashion.

In order to make our consideration as transparent as possible we, however, choose a simplified approximation, considering the wave reflection off a perfect conductor surface. In such a case, the boundary condition at the end of field line is $\mathbf{E} = 0$. On account of Eq. (6.14) one can derive the boundary condition $V_\varphi = 0$ at the ends of the magnetic field line. It should be noted that these relations can serve as proper boundary conditions rather for the sunlit ionosphere because of the high ionospheric conductivity at daytime.

The field line shape of the dipole magnetic field is described by Eq. (1.34). This equation relates the polar radius, r, to the magnetic latitude λ. If polar angle θ is

expressed through the magnetic latitude λ (northern hemisphere) via $\lambda = \theta - \pi/2$, the equation for magnetic field lines can be written as $r = LR_e \sin^2\theta$, where R_e is the mean Earth radius, L is the McIllwain parameter. In this notation the operator $\mathbf{B}_0 \cdot \nabla$ taken along the field line can thus be rewritten as

$$\mathbf{B}_0 \cdot \nabla = \frac{\mu_0 M_e}{4\pi L^4 R_e^4 \sin^7\theta} \frac{d}{d\theta}. \tag{6.16}$$

Substituting Eq. (6.16) for $\mathbf{B}_0 \cdot \nabla$ into Eq. (6.15) and rearranging yields (Dungey 1954, 1963; Cummings et al. 1969)

$$\frac{d}{d\theta}\left(\frac{1}{\sin\theta}\frac{d}{d\theta}\frac{V_\varphi}{\sin^3\theta}\right) + \frac{\rho\left(4\pi R_e^4\right)^2 L^8\omega^2 \sin^{10}\theta}{\mu_0 M_e^2} V_\varphi = 0. \tag{6.17}$$

We recall that the plasma velocity V_φ in Eq. (6.17) must be equal to zero at two intersection points where the corresponding field line crosses the bottom of the ionosphere. Substituting $r = R_e$ into Eq. (1.34) one can find the angles corresponding to these intersection points. We are thus left with the equation $\sin^2\theta_0 = \cos^2\lambda_0 = L^{-1}$ for the sought polar angles θ_0 and magnetic latitude λ_0. Finally, the proper boundary conditions for Eq. (6.17) take the form $V_\varphi(\theta_0) = V_\varphi(\pi - \theta_0) = 0$, where $\theta_0 = \arcsin L^{-1/2}$ and $\pi - \theta_0$ is the angle corresponding to the conjugate intersection point. The atmospheric depth is disregarded here.

Owing to the complexity of Eq. (6.17) the general analysis of this differential equation encounters some difficulty. As would be expected, considering the finite length of the field line segment bounded these two interception points, the given boundary problem has periodic solutions. The fundamental toroidal mode of Eq. (6.17) has numerically been studied by Dungey (1954, 1963). For example, according to this calculation made at the plasma density $\rho = 10^{-18}\,\mathrm{kg/m^3}$, the period of the fundamental mode can be approximated by the formula

$$T \approx \frac{0.6}{\sin^8\theta_0}, \quad \text{(in second)}. \tag{6.18}$$

Taking the numerical values of the magnetic latitude $\lambda_0 = 45°, 55°, 65°$ and $70°$, the typical periods of the fundamental mode are as follows: $T = 10\,\mathrm{s}, 54\,\mathrm{s}, 11\,\mathrm{min}$ and $55\,\mathrm{min}$, correspondingly, while the corresponding eigenfrequencies lie much below the IAR and Schumann resonances.

Thus, Eq. (6.17) describes the toroidal field oscillation in the magnetosphere or the standing shear quasi-Alfvén waves in the dipole approximation of the geomagnetic field. In this case the plasma velocity has only an azimuthal component and the "frozen in" magnetic field lines therefore vibrate within the resonance shell. The toroidal (twisting) oscillations manifest themselves through the azimuthal magnetic component and through the electric component orthogonal to the magnetic shell. Such quasi-Alfvén modes are referred to as the class of the FLRs.

6.1.3 Poloidal Mode

Now we consider another important mode of the magnetospheric oscillations, that is, the poloidal (breathing) mode, which contains the set of field components δB_r, δB_θ, V_r, V_θ, and E_φ. In contrast to the toroidal mode, which is mainly due to the shear Alfvén waves the poloidal mode is caused by the compressional waves, which propagate isotropically. To treat the basic properties of this mode we first take the azimuthal component of Eq. (6.7)

$$-i\mu_0\rho\omega E_\varphi = r^{-1}B_0^2\left[\partial_r\left(r\delta B_\theta\right) - \partial_\theta\delta B_r\right]. \tag{6.19}$$

As before all the functions are assumed to vary as $\exp(-i\omega t)$.

Maxwell equation $\nabla\times\mathbf{E} = i\omega\delta\mathbf{B}$ in spherical coordinates now is reduced to

$$\partial_\theta\left(\sin\theta E_\varphi\right) = i\omega\delta B_r r\sin\theta, \tag{6.20}$$

$$r^{-1}\partial_r\left(rE_\varphi\right) = -i\omega\delta B_\theta. \tag{6.21}$$

The set of Eqs. (6.19)–(6.21) can be solved for E_φ to yield the equation for poloidal mode

$$\frac{\omega^2 r}{V_A^2}E_\varphi + \partial_r^2\left(rE_\varphi\right) + \frac{1}{r}\partial_\theta\left[\frac{1}{\sin\theta}\partial_\theta\left(\sin\theta E_\varphi\right)\right] = 0. \tag{6.22}$$

Moreover the azimuthal plasma velocity $V_\varphi = 0$ while the components V_r and V_θ can be expressed through E_φ as follows:

$$V_r = -\frac{B_\theta}{B_0^2}E_\varphi, \quad V_\theta = \frac{B_r}{B_0^2}E_\varphi. \tag{6.23}$$

It follows from Eq. (6.23) that the scalar product of the poloidal mode velocity $\mathbf{V}_p = (V_r, V_\theta, 0)$ with $\mathbf{B}_0$ is equal to zero so that the plasma velocity $\mathbf{V}_p$ is perpendicular to the magnetic shell in contrast to the quasi-Alfvén oscillations. The poloidal mode is not guided by the field lines and can cover the whole magnetosphere or the large part of that. These modes are referred to as the class of cavity modes, which can propagate via FMS/compressional waves. In a homogeneous plasma, the phase velocity of the compressional waves is independent of the angle included between the plasma velocity vector and the geomagnetic field. Not surprisingly, the cavity oscillations due to compressional waves can fill the whole magnetosphere and the cavity mode spectrum is dependent on conditions at the outer boundary of the magnetosphere, that is, at the magnetopause.

Notice that the FMS/poloidal mode results in considerable variations of the field-aligned magnetic field, whereas the field-aligned electric current is small. On the contrary, the field-aligned current of the toroidal quasi-Alfvén mode has a finite value while the longitudinal magnetic field is small.

6.1.4 Azimuthal Harmonics

From the above analysis it is clear that in the axisymmetric magnetosphere model the basic equations can be split into two independent sets for the shear Alfvén and compressional waves, which can propagate independently of each other. According to the FLR theory, the magnitude of the standing shear Alfvén wave can reach a peak value in the vicinity of resonance magnetic shells under certain resonant conditions, whereas the standing compressional wave is associated with variations of the magnetic field perpendicular to the magnetic shells (Radoski 1967a; Radoski and Carovillano 1969; Southwood 1974; Chen and Hasegawa 1974; Krylov and Fedorov 1976; Krylov and Lifshitz 1984). In a general way, that is, in an arbitrary ambient magnetic field, the MHD-wave equations for these modes can be coupled. For example, if φ dependence of the normal modes is taken into account, all the functions should be expanded in a series of azimuthal harmonics $\exp(im\varphi)$, where $m = 0, 1, 2, \ldots$ is azimuthal wave number. Ignoring the φ dependence, we thereby have chosen $m = 0$ in the above equations. Furthermore, the shear and compressional Alfvén waves in the magnetospheric plasma can be coupled through the boundary conditions at the conducting E-layer of the ionosphere due to both the tensor character of the ionospheric plasma conductivity and finite value of Hall and Pedersen conductivities.

If $m \neq 0$ and $m \neq \infty$, the set of MHD equations for magnetospheric oscillations does not reduce to independent equations for the toroidal and poloidal modes. Nevertheless, away from the resonance magnetic shells the coupling between these modes is weak under the requirement that $m \sim 1$, and in the first approximation they can be considered as independent modes. The interactions between the toroidal and poloidal modes become significant only in a narrow region in the vicinity of the resonance shell (Leonovich and Mazur 1993; Leonovich 2000).

In the case of $m \gg 1$ the coupling between the shear Alfvén and compressional modes is so strong that they cannot be divided into two individual modes. Both of these modes manifest themselves as a single MHD mode, which is more likely to be similar to the Alfvén wave rather than to compressional one (Leonovich and Mazur 1993; Leonovich 2000). Nevertheless, such a quasi-Alfvén wave combines the properties of both modes, i.e., strong localization across the magnetic shell, that is typical for the shear Alfvén wave, and the presence of a considerable constituent of the field-aligned magnetic field variations, that is typical for the compressional wave.

If $m \to \infty$, the azimuthal scale across the main magnetic field tends to zero. This implies that the derivatives over φ in the MHD equations become much greater than those with respect to other variables. For this special case the MHD-wave equations can be split into two independent groups in analogy to the case of $m = 0$. As would be expected, considering the small value of the transverse scale, the plasma velocity V_φ is small and the plasma movement is mainly concentrated within the meridional plane (Dungey 1954, 1963).

6.2 Field-Line Resonance (FLR)

6.2.1 MHD Box Model

We now take up one more viewpoint on the magnetospheric resonances. To study the MHD-waves coupling in a little more detail, however, we need to consider a simple approximate model of the magnetosphere sketched in Fig. 6.1. In the model the dipole geomagnetic field lines are replaced by straightened field lines in such a way that the area marked in Fig. 6.1 with M is transformed into the parallelepiped/box magnetosphere shown in the bottom of Fig. 6.1. The y axis which was originally in the west–east direction is now transformed into a straight line that is infinite in length. In this picture the y-coordinate in the box model corresponds to the azimuthal direction/coordinate φ in the reference frame fixed to the Earth spin axis.

The box contains a cold magnetized plasma immersed in a straight magnetic field, $\mathbf{B}_0 = B_0(x)\,\hat{\mathbf{z}}$, which is a function of x. Both the plasma mass density, ρ, and the Alfvén velocity, V_A, also depend on only x, which plays a role of radial coordinate in the equatorial plane. The magnetic field lines are finite in length in the z direction and there are boundary conditions at the ends of lines. The box surfaces $z = 0$ and $z = l_1$ correspond to the southern and northern ionospheres. The box surface $x = 0$ represents the equatorial region of the ionosphere while the plane $x = l_2$ corresponds to the outer boundary of the magnetosphere. This model was originally suggested by Radoski (1966, 1967a,b) and has been termed the MHD box.

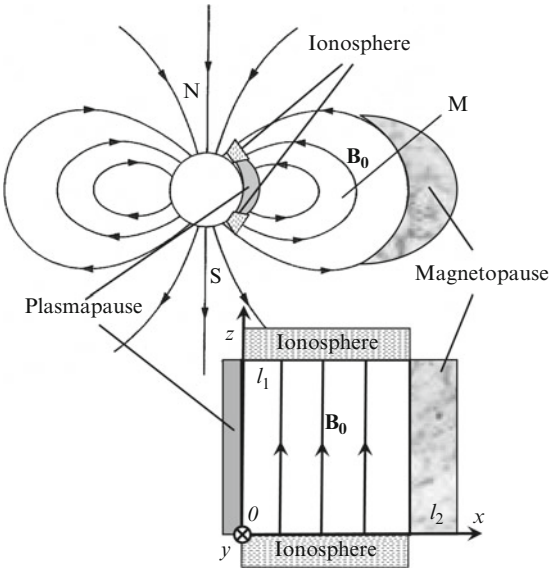

Fig. 6.1 Sketch of MHD-box model of the magnetosphere. The figure is partly adapted from Southwood and Kivelson (1982)

Plasma oscillations can be excited by sources situated both inside and outside the box. In order to take into account the internal source of excitation of the normal modes we now add the driven current, $\mathbf{J}_d$, to the conduction current on the right-hand side of Maxwell equation (1.5). The driven current is assumed to be a given function. Hence, Eq. (6.5) for the plasma motion is reduced to

$$\mu_0 \rho \partial_t \mathbf{V} = (\nabla \times \delta\mathbf{B}) \times \mathbf{B}_0 - \mu_0 (\mathbf{J}_d \times \mathbf{B}_0). \tag{6.24}$$

As is seen from Eqs. (6.3) and (6.24) the electric field $\mathbf{E}$ and the plasma acceleration $\partial_t \mathbf{V}$ are perpendicular to the unperturbed magnetic field $\mathbf{B}_0$. So we seek for the solution of the problem in the form $\mathbf{E} = \left(E_x, E_y, 0\right)$ and $\mathbf{V} = \left(V_x, V_y, 0\right)$. All perturbed quantities are considered to vary as $\exp\left(ik_y y\right)$, where k_y is the perpendicular wave number. Thus Eq. (6.24) is reduced to

$$\mu_0 \rho \partial_t V_x = \left(\partial_z \delta B_x - \partial_x \delta B_z - \mu_0 J_y\right) B_0, \tag{6.25}$$

$$\mu_0 \rho \partial_t V_y = \left(\partial_z \delta B_y - ik_y \delta B_z + \mu_0 J_x\right) B_0, \tag{6.26}$$

where J_x and J_y are the projections of the driven current $\mathbf{J}_d$.

In this approach the Faraday's law (1.2) reads

$$\partial_z E_y = \partial_t \delta B_x, \tag{6.27}$$

$$\partial_z E_x = -\partial_t \delta B_y, \tag{6.28}$$

$$ik_y E_x - \partial_x E_y = \partial_t \delta B_z. \tag{6.29}$$

The plasma velocity is related to the electric field through Eq. (6.3), that is

$$V_y = -E_x / B_0, \quad V_x = E_y / B_0. \tag{6.30}$$

Substituting V_x and V_y into Eqs. (6.25) and (6.26) we come to the set of equations for the electromagnetic fields. If $k_y = 0$, this set is split into two uncoupled sets of equation describing the shear Alfvén $\left(E_x, \delta B_y, V_y\right)$ and FMS waves $\left(E_y, \delta B_x, \delta B_z, V_x\right)$. A close analogy exists with axisymmetric magnetic field, in which, as we have noted, both the modes are uncoupled in an extreme case of azimuthal harmonics with $m = 0$. It should be noted that the first mode (E_x) corresponds to the toroidal field in the axisymmetric magnetosphere, whereas the second mode $\left(E_y\right)$ corresponds to the poloidal field.

Assuming that all the perturbed quantities vary in time as $\exp(-i\omega t)$ and solving this set of equations for E_x and E_y we come to the following wave equations:

$$\left(\partial_z^2 + \omega^2 / V_A^2\right) E_x = -i\mu_0 \omega J_x, \tag{6.31}$$

$$\left(\partial_x^2 + \partial_z^2 + \omega^2 / V_A^2\right) E_y = -i\mu_0 \omega J_y, \tag{6.32}$$

where

$$V_A(x) = \frac{B_0(x)}{[\mu_0 \rho(x)]^{1/2}}, \tag{6.33}$$

is the Alfvén velocity. Despite the fact that the wave equations (6.31) and (6.32) are independent, both the MHD modes can be coupled through the boundary conditions at the E region of the ionosphere. So we need to consider the effect of the boundary conditions on the spectrum of normal oscillations.

6.2.2 FLR Eigenfrequencies

For all frequencies of interest here the E region of the ionosphere can be considered as a thin conductive layer with integral Pedersen and Hall conductivities. The boundary condition (5.26) at the E layer relates the jump of horizontal magnetic field across this layer to the horizontal electric field. We recall that the interaction between the magnetospheric MHD waves and the ionosphere depends on value of the dimensionless parameters α_P and α_H, which are equal to the ratio of height-integrated Pedersen Σ_P and Hall Σ_H conductivities to the Alfvén wave parallel conductance of the magnetosphere $\Sigma_w = (\mu_0 V_A)^{-1}$. As would be expected, considering the FLRs due to the shear Alfvén waves propagation, the ionospheric Pedersen conductivity plays an important role in closing of the field-aligned Alfvén currents in the ionosphere, that is in the closing of the field lines perpendicular to **B**. In this picture the Hall conductivity in the ionosphere is of minor importance and in the first approximation it can be ignored (e.g., Krylov and Fedorov 1976; Krylov and Lifshitz 1984). In this approach the wave perturbations coming from the magnetosphere cannot penetrate through the conducting ionosphere so that we can neglect the variations of the magnetic field below the ionosphere. In this way the boundary condition (5.26) at the ionosphere reduces to

$$\delta B_y = \pm \mu_0 \Sigma_P^{\pm} E_x, \quad \text{and} \quad -\delta B_x = \pm \mu_0 \Sigma_P^{\pm} E_y, \tag{6.34}$$

where the sign plus on the right-hand side of Eq. (6.34) corresponds to the northern ionosphere ($z = l_1$) and the sign minus corresponds to the southern ionosphere ($z = 0$). Furthermore, Σ_P^+ stands for the height-integrated Pedersen conductivity of the northern ionosphere while Σ_P^- denotes the same value for the southern ionosphere. Combining Eqs. (6.27), (6.28), and (6.34) we finally obtain

$$\partial_z \mathbf{E}_\perp = \pm i\omega\mu_0 \Sigma_P^{\pm} \mathbf{E}_\perp, \tag{6.35}$$

where $\mathbf{E}_\perp = \left(E_x, E_y\right)$ and $z = 0$ or l_1.

We choose first to study the free Alfvén oscillations at $J_x = 0$. In such a case the solution of Eq. (6.31) can be written

$$E_x = C_1 \exp(i\omega z/V_A) + C_2 \exp(-i\omega z/V_A), \tag{6.36}$$

where C_1 and C_2 are undetermined constants. Substituting Eq. (6.36) for E_x into boundary conditions (6.35) we come to an algebraic set of equations for constants C_1 and C_2. This set of equations has a nontrivial solution under the requirement that the system determinant equals to zero, whence it follows

$$\exp\left(-\frac{2i\omega l_1}{V_A}\right) = R_+ R_-, \tag{6.37}$$

where

$$R_+ = \frac{1-\alpha_P^+}{1+\alpha_P^+} \quad \text{and} \quad R_- = \frac{1-\alpha_P^-}{1+\alpha_P^-} \tag{6.38}$$

denote the reflection coefficients for the northern and southern ionospheres, respectively. These coefficients vary from 1 to -1 with changing $\alpha_P^{\pm}$ from zero to infinity.

Decomposing the frequency in Eq. (6.37) into its real and imaginary parts, $\omega = \omega' + i\omega''$, one finds the solution of Eq. (6.37) in the form

$$\omega_n'(x) = \pi n V_A(x)/l_1, \tag{6.39}$$

when $R_+ R_- > 0$ and

$$\omega_n'(x) = \{\pi V_A(x)/l_1\}(n-1/2), \tag{6.40}$$

when the inverse inequality, $R_+ R_- < 0$, is valid. Here n is integer, $n = 1, 2, \ldots$ In both of these cases the imaginary part of the frequency is given by

$$\omega''(x) = \frac{V_A(x)}{2l_1} \ln|R_+ R_-|. \tag{6.41}$$

If $k_y \neq 0$, the general solution and eigenfunctions of the problem are found in Appendix F. In this case the normal modes are coupled through the boundary conditions at the conjugate ionospheres. The sole exception corresponds to two opposite extreme cases of zeroth and infinite Pedersen conductivities when the shear Alfvén and FMS modes become independent. In these extreme cases the wave vector $k_n = \omega_n'/V_A$ in Eq. (6.39) coincides with that given by Eq. (6.125).

The general solution of the problem can be expanded in a series of the orthonormal eigenfunctions, $q_n(z)$, given by Eq. (6.126). Arbitrary perturbations of E_x and δB_y appear as a sum of modes, each of which changes harmonically in time. Considering the amplitudes E_{xn} and δB_{yn} of the normal oscillation with frequency $\omega = \omega_n(x)$ and rearranging Eq. (6.126) we get

$$E_{xn} \propto q_n = \frac{\sin k_n z}{k_n} + \frac{i\cos k_n z}{k_n \alpha_P^-}, \quad \delta B_{yn} \propto \frac{dq_n}{dz}, \tag{6.42}$$

where $k_n = \omega_n / V_A = \left(\omega_n' + i\omega''\right) / V_A$ is not a function of x and the real and imaginary parts of ω are given by Eqs. (6.39)–(6.41).

As long as x is fixed, Eqs. (6.39)–(6.41) describe the spectrum of normal Alfvén oscillations. It should be emphasized that this spectrum depends on x and thus is continuous. The real part of the frequency $\omega_n'(x)$ represent the eigenfrequency of the n-th harmonic. Notice that all the eigenfrequencies are equidistant, whereas the damping factor $\omega''(x)$ is independent of n. From these equations it is clear that the magnetic shell which has a constant value of x will vibrate as a whole. In this picture all the segments of the field lines at constant x will covibrate so that it is sufficient to study the normal oscillations of one of these field lines. The net Alfvén perturbations can be thus considered as a superposition of the independent normal oscillations of the field lines/magnetic shells.

It is clear that Eq. (6.39) describes the frequencies of the half-wave mode in such a way that an integer number of half-waves lies on the field line while Eq. (6.40) corresponds to the quarter-wave mode. In this case the field line length equals to $1/4, 3/4, 5/4 \ldots$ of the wavelength.

This kind of field line oscillations has a close analogy with normal oscillations of a taut elastic string. The sense of the magnetic force is similar to that of elastic forces due to tension in a stretched string since the restoring force in Alfvén oscillations arises due to tension in the magnetic field line. In addition, the shear Alfvén waves play a role of the transverse elastic waves propagating along the string.

In the framework of the "MHD-box" model, we note that the energy loss is mostly due to the Joule dissipation at the ends of field lines, that is in the ionosphere. The interpretation we make is that the Joule dissipation results from the Pedersen conductivity, which is subject to diurnal variations. It is usually the case that at the nighttime ionosphere Σ_P is much smaller than Σ_w so that the parameter α_P is small. On the contrary, at the dayside ionosphere the plasma conductivity is so high that α_P is greater than unity.

Consider first the extreme case of a small Pedersen conductivity in the conjugate ionospheres when α_P tends to zero at both ends of the field line, that means that $R_+ R_- > 0$. From here it follows that the set of eigenfrequencies, $\omega_n'(x)$, is described by Eq. (6.39), while the damping factor, $\omega''(x)$, in Eq. (6.41) tends to zero. As it is seen from Eq. (6.42), in this case $\partial_z E_x = 0$ at the ends of field line. This means that the transverse electric field E_x has a node in the equatorial plane and it has the antinodes at the ends of the field line. The same is true for the plasma velocity V_y, which is related to E_x through Eq. (6.30). On the contrary, it follows from Eq. (6.42) that the transverse magnetic field δB_y has the nodes at the ends of the field line. To illustrate this, the symmetrical profiles of the first and second harmonics of δB_y are shown in Fig. 6.2 with solid ($n = 1$) and dotted ($n = 2$) lines.

Before leaving this case it is useful to return to the analogy between the field lines and elastic strings. Considering the taut elastic string dead at its two ends and replacing V_A by the velocity of the elastic wave, we note that Eq. (6.39) can describe the eigenfrequencies of the elastic string with the length l_1.

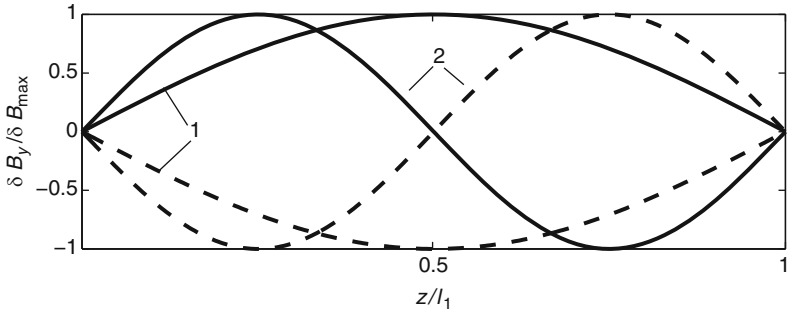

Fig. 6.2 Profiles of the standing Alfvén waves at the magnetospheric shell in the extreme cases $\alpha_P^{\pm} \to 0$. The first and second harmonics of the transverse magnetic field δB_y are shown with *solid* ($n = 1$) and *dotted* ($n = 2$) *lines*

In the inverse case of $\alpha_P^{\pm} \to \infty$, the set of eigenfrequencies is defined by Eq. (6.39) as before. Moreover, the damping factor in Eq. (6.41) is equal to zero as well. In this case $E_x = 0$ at the ends of field line. The interpretation we make is that the Joule dissipation of energy in the ionosphere can be neglected since the electromagnetic field cannot penetrate into the ionosphere due to its infinite conductivity. The components E_x and V_y have an antinode in the equatorial plane and the nodes at the ends of the field line, whereas δB_y has the antinodes at the ends of the field line. Notice that the analogous eigenfrequencies have the elastic string dead in its middle.

If $\alpha_P^{\pm}$ is finite and nonzero, Eqs. (6.39)–(6.41) generally describe the spectrum of damped Alfvén oscillations, which are similar to oscillations of the stretched elastic string with energy losses at the claimed end points.

If a homogeneous confined space is studied, it is usually the case that the spectrum of normal field oscillations is discrete. On the basis of the "MHD-box" model, we have found, however, that the spectrum of the Alfvén oscillations is continuous. It is not surprising that there is one-dimensional (1D) inhomogeneity across straight field lines. In some sense, the actual Earth magnetic field is inhomogeneous across the magnetic shells. This implies that the spectrum of the FLR of the Earth magnetic field depends on the magnetic shell, which is a function of the McIllwain parameter L. Under nominal magnetospheric conditions one may expect an increase of the oscillation period with L or with radial distance, at least at auroral latitude. Below we show that this conclusion is consistent with the observations. It can be shown that in a curvilinear magnetic field the major features of the FLR are the same except for the effect of polarization splitting of the FLR-spectrum. This effect is due to the difference of the convergency/divergency rate of the magnetic field lines within the meridional and equatorial plains. The interested reader is referred to the text by Leonovich and Mazur (1993) and Leonovich (2000) for details about the dependence of the FLR-resonance frequencies on polarization.

6.2.3 Cavity Mode

In this section we consider as before $k_y = 0$ in order to treat each wave mode separately. In a cold homogeneous plasma the phase velocity of the compressional/FMS wave is independent of the angle between the wave vector $\mathbf{k}$ and the external magnetic field $\mathbf{B}_0$. In the MHD box model the properties of this mode are defined by Eq. (6.32), which is an ordinary 2D (two dimensional) wave equation for an inhomogeneous plasma. This means that in contrast to the Alfvén waves which are guided by the field lines, the compressional waves can propagate in all directions and fill the whole resonance cavity. In the magnetosphere these waves are therefore referred to as the class of cavity modes.

We will seek for the solution of Eq. (6.32) in terms of the series

$$E_y = \sum_n A_n(x)\, q_n(z), \tag{6.43}$$

where the orthonormal eigenfunctions $q_n(z)$ of the problem are given by Eq. (6.126). These eigenfunctions satisfy the boundary conditions (6.34) at the southern ($z = 0$) and at the northern ionospheres ($z = l_1$). Substituting Eq. (6.43) for E_y and Eq. (6.126) for q_n into Eq. (6.32) yields

$$\sum_{m=1}^{\infty} \left\{ A_m'' + \left(k_A^2 - k_m^2\right) A_m \right\} q_m = -i\mu_0 \omega J_y, \tag{6.44}$$

where $k_A(x) = \omega / V_A(x)$, and the prime denotes derivative with respect to x. The eigenvalues $k_n(\omega)$ are the roots of Eq. (6.123). In two extreme cases of the non-conducting ionosphere $\left(\Sigma_P^{\pm} = 0\right)$ and of the perfect conducting ionosphere $\left(\Sigma_P^{\pm} \to \infty\right)$ there are only real roots

$$k_n = \pi n / l_1, \quad \text{where } n = 1, 2, 3 \ldots, \tag{6.45}$$

which are independent of the frequency ω. Overall, if the Pedersen conductivities $\Sigma_P^{\pm}$ are finite and nonzero values, the eigenvalues are complex.

Consider first the problem of free oscillations assuming for the moment that $J_y = 0$. Multiplying both sides of Eq. (6.44) by $q_n(z)$, integrating these equations over z from 0 to l_1 and using the condition (6.127) of orthogonality of the eigenfunctions $q_n(z)$, we come to

$$A_n'' + \kappa^2 A_n = 0, \tag{6.46}$$

where

$$\kappa^2(x) = k_A^2(x) - k_n^2(\omega). \tag{6.47}$$

The plasma velocity normal to the boundaries of equatorial ionosphere and magnetopause is assumed to be equal to zero, that is $V_x = 0$ at $x = 0$ and $x = l_2$. From Eq. (6.30) it follows that E_y and A_n are both zero at $x = 0$ and $x = l_2$. Equation (6.46) under this homogeneous boundary condition is a special case of the so-called Sturm–Liouville problem for determination of the resonance frequencies of the cavity mode. To estimate the fundamental frequency of the normal oscillations, consider the case of constant Alfvén speed when the parameter κ in Eq. (6.47) is independent of x. The solution of Eq. (6.46) can be thus written as $A_n = C_n \sin \kappa x$, where C_n is the undetermined constant. Under boundary conditions alluded to above the parameter κ is given by an equation similar to Eq. (6.45), that is

$$\kappa_m = \pi m / l_2, \tag{6.48}$$

where m is integer. For simplicity, the eigenvalues $k_n(\omega)$ is assumed to be given by Eq. (6.45). Combining this equation with Eqs. (6.47) and (6.48) we obtain the set of resonance frequencies

$$\omega_{n,m} = V_A \left(\frac{n^2}{l_1^2} + \frac{m^2}{l_2^2} \right)^{1/2}. \tag{6.49}$$

In the framework of the MHD box model the curvature of Earth magnetic field is ignored. To give a numerical estimate of the fundamental eigenfrequency ($n = m = 1$), it is necessary at this point to find a suitable estimate of the parameters appearing in Eq. (6.49). We recall that the x axis approximates the radial direction. If the outer boundary of the magnetosphere $l_2 = LR_e$ corresponds to the McIllwain parameter $L \approx 5$, the corresponding length of the field line $l_1 \approx 7.7R_e$. Substituting the Earth radius $R_e = 6.4 \times 10^3$ km and the Alfvén speed $V_A = 10^3$ km/s into Eq. (6.49), we get $f_{11} = \omega_{11}/(2\pi) \approx 0.02$ Hz. The cavity resonance period of the fundamental harmonic is about $T_{11} = f_{11}^{-1} \approx 50$ s. It should be noted that we have obtained only the rough estimate of the period and frequency of the fundamental harmonic.

As would be expected, an FMS-wave in the magnetosphere may increase in amplitude as the wave frequency is close to the frequencies of the global resonances. This kind of oscillations can cover a significant part of the magnetosphere. In the framework of the MHD box model the properties of the cavity mode are similar to that of the TE mode excited in the inhomogeneous resonator. Since the y direction corresponds to the azimuthal coordinate of the magnetosphere, the transverse electric field E_y corresponds to the azimuthal component E_ϕ. In some sense, the cavity mode is identical in its properties to the poloidal mode in the curved magnetic field. Some concerns about the mode coupling and the energy dissipation are found in the next sections.

6.2.4 The Mode Coupling

In this section we consider the field variations excited by the plasma perturbations coming from the outer space into the magnetosphere. Such perturbations can be resulted from the interaction between the solar wind and the Earth's magnetic field at the magnetopause. The curvature of the magnetospheric boundary is ignored since the perturbations wavelength is assumed to be much smaller than the size of the magnetospheric cavity. The MHD box model of the medium is a reasonable approximation at this point to proceed analytically and to treat the FLR structure.

The inner region of the magnetosphere is assumed to be free of the driving/external current so that $J_y = 0$. To specify the problem, we assume that E_y is a given function at the magnetospheric boundary $x = l_2$. As one example, let $E_y = E_0(z)\exp\left(-i\omega t + ik_y y\right)$ at the box surface $x = l_2$ while $E_y = 0$ at $x = 0$. This function can describe the perturbation coming from outer space into the magnetosphere or the surface wave generated at the magnetopause. Here ω is the frequency of this wave. (In general ω is a complex value.) The inhomogeneous boundary conditions at $x = l_2$ are important in the sense that they play a role of source of field variations in the magnetosphere.

If $k_y = 0$, then the shear Alfvén and compressional waves are described by independent Eqs. (6.31)–(6.32). As before we seek for the solution for E_y in terms of the series (6.43) in eigenfunctions $q_n(z)$ where the expansion coefficients $A_n(x)$ satisfy the differential equation (6.46). If the boundary function $E_0(z)$ can be expressed as a series of eigenfunctions $q_n(z)$, that is

$$E_0(z) = \sum_n d_n q_n(z), \tag{6.50}$$

then the expansion coefficients are given by

$$d_n = \int_0^{l_1} E_0(z)\, q_n(z)\, dz. \tag{6.51}$$

Whence it follows that the boundary conditions reduce to $A_n(0) = 0$ and $A_n(l_1) = d_n$.

We will study Eq. (6.46) by using a qualitative method since the explicit form of the function $V_A(x)$ is unknown. As is seen from Eq. (6.33), the Alfvén speed depends on both the Earth magnetic field $\mathbf{B}_0$ and the plasma density. The plasma density falls off more rapidly with distance x than $\mathbf{B}_0$ does, and hence the Alfvén speed generally increases with distance. At the outer boundary of the magnetosphere ($x = l_1$) the Alfvén speed is on one or two order of magnitude greater than that at the conducting layer of the ionosphere ($x = 0$). Furthermore, if near the boundary $x = l_1$ the wave frequency is so small that the inequality $\omega / V_A(x) \ll |k_n(\omega)|$ takes place, then the parameter κ in Eq. (6.46) is approximately constant. This means

that the exponential functions can fit the approximate solutions of Eq. (6.46) in this region. For example, considering for the moment that V_A is a constant, we get

$$A_n = d_n \frac{\sinh \lambda_n x}{\sinh \lambda_n l_1}, \quad \text{where} \quad \lambda_n = \left(k_n^2 - k_A^2\right)^{1/2}. \tag{6.52}$$

It follows from this equation that the boundary perturbations E_y decay in amplitude with decreasing the distance x due to the exponential fall off of all the coefficients A_n. The interpretation we make is that the FMS waves must attenuate when propagating from the outer boundary to the inner region of the magnetosphere. This tendency is valid for the case of space-varying Alfvén speed except for the region where the FLR occurs.

In the resonance region the coupling of the shear Alfvén and the FMS waves cannot be ignored. The mode coupling is studied in more detail in Appendix F. As we have noted above, if $k_y \neq 0$, then Eqs. (6.25)–(6.29) cannot be split into two independent sets of equations. In this case the FMS wave can excite the shear Alfvén wave and vice versa. The interaction between these two modes may greatly affect the field amplitude as the resonance condition

$$k_A^2(x) = k_n^2 \tag{6.53}$$

holds true. If $x = \xi$ is a root of Eq. (6.53), then at this point the wave frequency ω equals to one of the Alfvén resonance frequencies $\omega_n(x)$ that are given by Eqs. (6.39)–(6.41).

As has already been stated in Appendix F, the amplitude the Alfvén mode which includes the components δB_y, E_x, and V_y, has a peak of Lorentz form near the FLR position $x = \xi$. The schematic representation of the amplitude of δB_y as a function of x/ξ is displayed in Fig. 6.3 with solid line 1. According to Eqs. (6.139) and (6.141), the amplitude of the components δB_x, E_y, and V_x has a maximum at the same resonance point but this maximum is not so distinct as is shown in Fig. 6.3 with dashed line 2. It is worth mentioning that, as shown in Appendix F, the phase of the resonance components E_x and δB_y, changes by π when crossing the maximum.

The next singular point $x = \eta$, can be found from the following equation

$$k_A^2(x) = k_n^2 + k_y^2. \tag{6.54}$$

The implication here is that the roots of this equation correspond to turning points $x = \eta$ where solutions change from being oscillatory in nature to characteristically growing or decaying with coordinate x. At the turning point the wave reflection occurs. It should be noted that if $V_A(x)$ is not a monotonic function there may be more turning and resonance points.

The MHD box model is based on an idealized field geometry that ignores the magnetic field line curvature and dip angle but includes the field variations with radial distance and boundary conditions at the ionosphere and magnetopause. The MHD box model provides us with a qualitative theory of the FLR in the

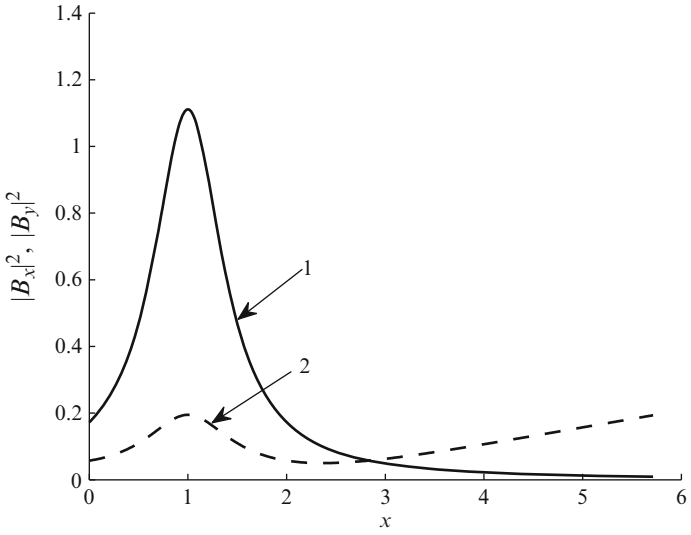

Fig. 6.3 The perpendicular magnetic field components in the vicinity of field line resonance position versus normalized variable x/ξ_n. The components $|\delta B_y|^2$ and $|\delta B_x|^2$ are shown with *solid line 1* and *dashed line 2*, respectively

magnetosphere. We recall that in the model the coordinate x plays a role of the radial distance in the actual magnetosphere. In this picture the resonance components, δB_y and E_x, are analog of the azimuthal magnetic field variations and the radial electric field variations, respectively. A schematic plot of the amplitude variations as a function of L-shell is shown Fig. 6.4.

As one example, consider the MHD wave excited due to, say, plasma instabilities at the magnetopause. A scheme of penetration of MHD wave from the magnetospheric boundary into its inner region can be summarized as follows. At first the initial perturbations propagate as an FMS-wave from the magnetospheric boundary to the turning point where wave reflection occurs. The electromagnetic field in this region may be oscillatory in character. Once the turning point has been passed, the amplitude of the FMS-wave falls off exponentially with distance up to the region where the FLR conditions will occur. This implies that in this region the wave frequency becomes close to the Alfvén resonance frequency of the magnetic shell. In the vicinity of the resonance shell the energy of the FMS-wave is transferred in part into the energy of the Alfvén oscillations by virtue of the mode coupling to the shear Alfvén and FMS modes. The shear Alfvén wave can get trapped in this region thereby exciting the FLR. At the resonance point a phase shift of π between the toroidal field components (δB_y and E_x in the box model) on both sides of the resonance is apparent. Some complication arises in this scenario as there are several turning points or resonance shells.

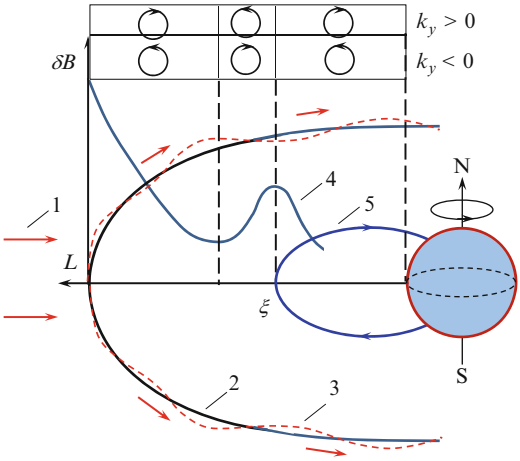

Fig. 6.4 A schematic plot of amplitude variations of FMS wave excited at the magnetopause and sense of the wave polarization as a function of L-shell in the magnetosphere. *1*—solar wind, *2*—magnetopause, *3*—boundary surface wave caused by Kelvin–Helmholz instability, *4*—plot of wave amplitude, *5*—resonance field line

Attenuation of the resonance oscillation is basically due to the Joule dissipation caused by the Pedersen conductivity in the ionosphere. In addition, azimuthal propagation of the waves leads to the energy losses in the magnetotail.

The Hall conductivity scarcely affects the FLR but it may play a crucial role in occurrence of the magnetic perturbations under the ionosphere, that is in the atmosphere and on the ground surface. As the Hall conductivity is ignored, the incident shear Alfvén wave cannot excite the field perturbation in the atmosphere. If only the Hall conductivity is finite, the shear Alfvén wave can be transformed in the ionosphere into both the reflected and transmitted field of the FMS wave. In other words, the FLR-related field observed on the ground builds up as a result of the mode coupling in the ionosphere via the Hall conductivity followed by the penetration of the FMS mode through the atmosphere towards the ground.

A variety of mechanisms of coupling between the shear Alfvén and FMS waves in a realistic magnetospheric environment have been studied in numerous papers. With some care the terms “shear Alfvén wave” and “FMS” are applicable to the actual MHD waves propagating in the magnetosphere since in most cases these pure eigenmodes do not exist. However these two terms are extremely important for understanding of wave processes in the planetary magnetosphere. The interested reader is referred to the text by Glassmeier (1995) for a more complete review on mode coupling in actual magnetosphere.

6.2.5 *Wave Polarization*

As we have noted above, near the resonance the phase of the resonance components changes by π abruptly, so one may expect a corresponding change in the wave polarization in the vicinity of the resonance point. From Eq. (6.131) it follows that the amplitudes of E_x and E_y are related through

$$\frac{E_x}{E_y} \sim \frac{ik_y}{\left(k_A^2 - k_n^2 - k_y^2\right)} \frac{dE_y}{dx} \frac{1}{E_y}. \tag{6.55}$$

In the region $x < \eta$ the sense of polarization depends on only the signs of k_y and dE_y/dx. In other words, the sense of polarization is a function of the direction of propagation in y, and it depends on whether the amplitude increases or decreases with the radial distance (Southwood 1974).

In the vicinity of the resonance point $x = \xi$ Eq. (6.55) is reduced to

$$\frac{E_x}{E_y} \sim -\frac{i}{k_y} \frac{dE_y}{dx} \frac{1}{E_y}. \tag{6.56}$$

This implies that the sense of polarization switches on each side of a maximum and or minimum in amplitude. For example, consider an eastward propagating MHD wave, which corresponds to $k_y > 0$. In the region where $dE_y/dx < 0$ the wave is the clockwise-polarized and vice versa. We recall that the y axis corresponds to the west–east direction, while x axis is in radial direction. In this picture the expected polarization and the wave amplitude as a function of L for magnetic equator plane is schematically shown at the upper panel of Fig. 6.4. For the resonance shell the polarization tends to be linear. In the case of a westward propagating wave $\left(k_y < 0\right)$ the sense of polarization is reversed. Looking down on the Earth from above in the northern hemisphere, this wave would have clockwise polarization south of the resonant site ξ and anticlockwise polarization north of the resonance. These properties of the polarization would thus be expected to be valid on the ground despite the influence of the conducting E layer of the ionosphere.

On the basis of data recorded at a chain of stations at geomagnetic latitudes between 59°N and 77°N within 2° of longitude 302°E Samson et al. (1971) have studied the diurnal and latitude variations of the amplitude and polarization of the long-period pulsation. Their basic results for fixed frequency of 5 mHz are schematically shown in Fig. 6.5. The pulsation amplitude reaches a peak value at the line which belongs to auroral zone. Across this line the rotation sense of the horizontal polarization changes from counterclockwise to clockwise or vice versa at midday.

It is generally believed that the ULF pulsations in the frequency range 10^{-2}–10^{-3} Hz originate from the interaction between the solar wind and planetary magnetosphere. In this picture an FMS wave propagating in the magnetosphere can build up as a result of Kelvin–Helmholtz instability at the magnetopause.

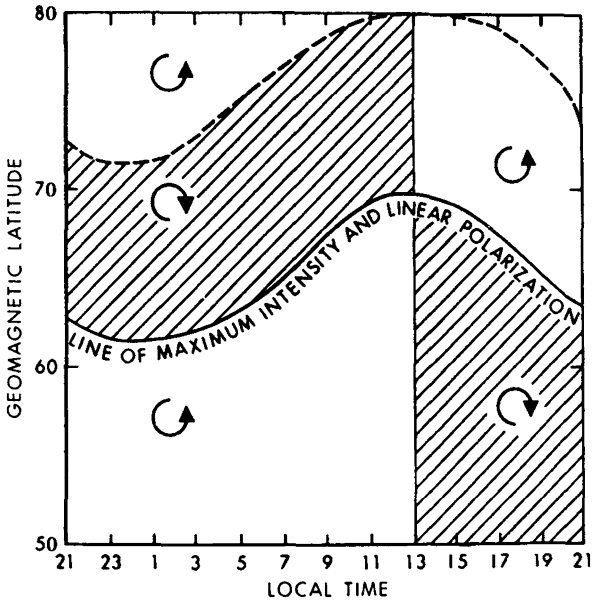

Fig. 6.5 A schematic plot of the diurnal and latitudinal variations of the amplitude and sense of rotation of the horizontal component for 5 mHz pulsations as observed by Samson et al. (1971). The amplitude of the pulsations reaches a peak value at auroral zone, with latitude changing in local time as shown with line of maximal intensity. The horizontal polarization switches sense across this line. Taken from Glassmeier (1995)

When propagating from the magnetopause into the magnetosphere the FMS wave decays in amplitude until the resonance point will occur, as shown in Fig. 6.4. The switch in polarization at this point is consistent with waves propagating eastwards $(k_y < 0)$ in the afternoon and westwards $(k_y > 0)$ in the morning. On account of the fact that the radial derivative of the azimuthal electric component (dE_y/dx in the MHD-box model) changes sign across the resonant point, a four-quadrant pattern arises due to the FLR phenomenon much as observed by Samson et al. (1971) (Fig. 6.5).

6.2.6 *Effect of the Ionosphere on Ground-Based Observation*

As has already been stated, the amplitude of the FMS-waves falls off exponentially as they propagate towards the ionosphere and their amplitude becomes smaller than that of Alfvén waves. This means that the polarization of the MHD waves incident to the ionosphere can be considered to be basically corresponding to that of Alfvén mode.

The ionospheric plasma may greatly affect the ground-based observation of the ULF pulsations. The dominant effect is the attenuation of MHD waves and rotation

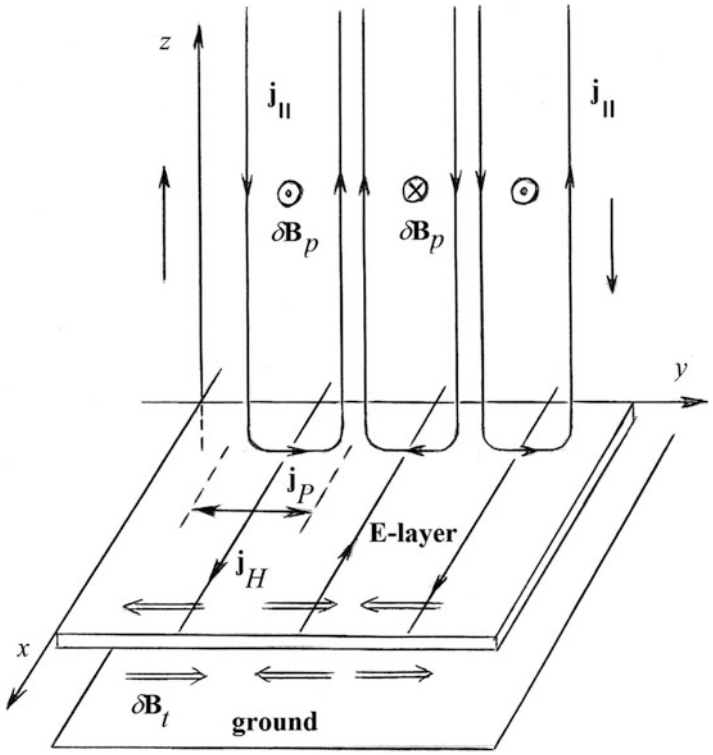

Fig. 6.6 A schematic illustration of the electric current system and magnetic perturbations resulted from Alfvén wave interaction with the ionosphere

of polarization mainly due to the conducting E layer of the ionosphere. The high frequency range of the signal spectrum undergoes strong attenuation since the skin length of the conducting ionosphere is inversely proportional to the square root of frequency. In other words, the ionosphere acts as a spatial low-pass filter for the signals observed on the ground.

To illustrate the rotation of polarization, we will consider the effect of an incident Alfvén wave on the high-latitude ionosphere. To make our consideration as transparent as possible, the Earth magnetic field is assumed to be homogenous and positively parallel to vertical z axis. A plane harmonic Alfvén wave propagates along the magnetic field perpendicular to the ionosphere that are in the plane x, y. All perturbed values are assumed to vary as $\exp(iky - i\omega t)$. In the magnetosphere the Alfvén wave carries transverse polarization of electromagnetic perturbations and field-aligned current, $\mathbf{j}_{\parallel}$, as schematically shown in Fig. 6.6. The conducting E layer of the ionosphere shorts out the field-aligned current thereby exciting the sheet current system. As the magnetic $\delta\mathbf{B}$ and the electric $\mathbf{E}$ perturbations in the magnetosphere are directed along the x and y axes, respectively, the Pedersen current $\mathbf{j}_P = \sigma_P\mathbf{E}$ in the E layer of the ionosphere is parallel to y axis while

the Hall current $\mathbf{j}_H = \sigma_H (\hat{\mathbf{z}} \times \mathbf{E})$ is parallel to x axis. The Pedersen and the Hall conductivities of the E layer are assumed to be constant.

Thus the field-aligned currents of the incident and reflected Alfvén waves and the ionospheric sheet system of currents, shown in Fig. 6.6, can be split into poloidal and toroidal current systems. The first one includes the field-aligned currents and the ionospheric Pedersen currents. In such a case the magnetic perturbation, $\delta\mathbf{B}_p$, are concentrated inside the poloidal current system so that the magnetic effect is undetectable below the ionosphere. In general, formal proof of this assertion can be found in McHenry and Clauer (1987). The toroidal system builds up as a result of the Hall currents flowing in the E layer of the ionosphere. In our model these currents are closed in the infinity ($x \to \pm\infty$). The magnetic field of the toroidal currents, $\delta\mathbf{B}_t$, is perpendicular to $\delta\mathbf{B}_p$. This means that the magnetic perturbations in the atmosphere are perpendicular to the magnetospheric field of the Alfvén wave. The ionosphere therefore changes the wave polarization by 90°. In our model we have ignored the field line curvature and the inhomogeneous distribution of the Pedersen and Hall conductivities in the ionosphere. Actually the ionosphere produces a rotation of the polarization plane in the angle range from 0° to 90°. The detailed calculations of this problem are found in numerous papers (e.g., see review by Glassmeier 1995 for details). Notice that the latitude variations of the ULF pulsation period, as observed in space and on the ground, are in favor of the ionospheric rotation effect. In particular the latitude dependence of the Alfvén resonance oscillations in space is detected in azimuthal component (D component), whereas the ground-based observation exhibits the same dependence in meridional field (H component) that is consistent with the rotation of components by the angle 90°.

6.3 Sources of ULF Pulsations

6.3.1 Observations of ULF Pulsations

Observations and study of ULF MHD waves is certainly necessary as they transmit energy, momentum, and most importantly they provide us with information about magnetospheric dynamics. A variety of these waves occurring in the magnetosphere and ionosphere result in the generation of ULF geomagnetic pulsations that have been identified in both ground-based and satellite observations. Periods and frequencies of the ULF pulsation vary from 0.2 to 600 s, and from several milliHertz to several Hertz, respectively. Below is the frequency range of magnetic storms. The amplitudes of the ULF pulsation typically change from 0.1 to 50 nT.

In standard geophysical practice the ULF pulsations are classified according to their period. They can be also divided into two classes depending on whether the pulsation accompany substorms or not (e.g., see Jacobs 1970; Nishida 1978). The latter class includes the regular quasiharmonic oscillations, which are termed Pc oscillations (Pulsations continuous). This class of the ULF pulsations can be in turn

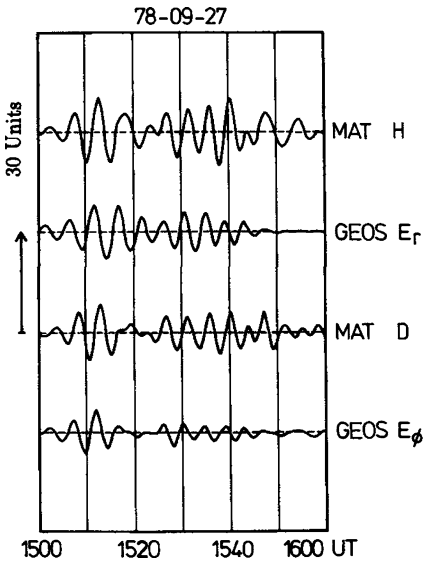

Fig. 6.7 A Pc5 pulsation event recorded at the ground-based observatory of the Scandinavian Magnetometer Array in the Finmark (shown with MAT) and in the magnetosphere by the geostationary satellite GEOS 2 (shown with GEOS). The H and D components of the magnetic variations have been recorded at the ground-based station while the components of electric variations, E_r and E_ϕ, were measured on board the satellite. Units of the magnetic and electric variations are nT and 0.1 mV/m, respectively. Taken from Glassmeier (1995)

split into five spectral subclasses Pc1 (period 0.2–5 s), Pc2 (5–10 s), Pc3 (10–45 s), Pc4 (45–150 s), and Pc5 (150–600 s). The period of the Pc oscillations are controlled by both the parameters of interplanetary space and the resonance properties of the Earth magnetosphere. The class of irregular pulsations, which have been termed Pi pulsations (Pulsations irregular), consists of two subclasses Pi1 (1–40 s) and Pi2 (40–150 s). These pulsations are a signature of onset of magnetospheric substorms which build up as a result of the plasma and solar energy penetration into the magnetosphere from the interplanetary space during magnetic storms and active processes on the Sun. Certainly, this classification is fairly relative. There are complicated and unusual pulsations, in which the regular and irregular oscillations are mixed.

The typical amplitude of Pc5 pulsations, about 10–50 nT, is the largest among the ULF pulsation. An example of Pc5 pulsations simultaneously observed at the ground-based station and in the magnetosphere by the geostationary satellite GEOS 2 is shown in Fig. 6.7 (Glassmeier 1995). This event is in favor of the magnetospheric origin of the Pc5 pulsations. The Pc5 pulsations are latitude-dependent and are frequently localized within narrow regions extended along geomagnetic parallels. It is usually the case that the period of the Pc5 pulsation falls off with decreasing latitude of the sighting point (Ohl 1962, 1963; Annexstad and

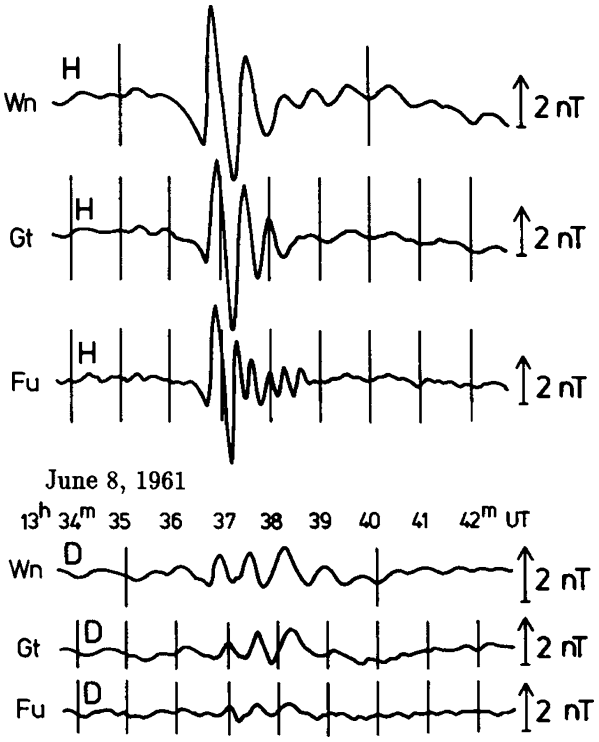

Fig. 6.8 Large-scale ULF pulsations observed at the geomagnetic observatories Wingst (Wn), Göttingen (Gt), and Fürstenfeldbruck (Fu). H and D components of the magnetic variations are displayed in the upper and bottom panels, respectively. Taken from Voelker (1962), and Glassmeier (1995)

Wilson 1968). This property keeps partly for the case of Pc4 pulsation. It should be noted that at the latitudes below $50° - 60°$ these pulsations can be masked by the global magnetic variations with time-independent period. The fundamental Pc5 pulsations occur primary in the sunlit hemisphere. This asymmetry probably arises from magnetospheric structure asymmetries, which result from the existence of the magnetotail and the plasmospheric convexity in the nightside magnetosphere.

The damped-type Pc3–Pc4 oscillations of global extension are illustrated in Fig. 6.8 (Voelker 1962). These oscillations with latitude-dependent period have been recorded at three ground-based stations located at Wingst (the northernmost station), Göttingen, and Fürstenfeldbruck (the southernmost station). The increase of the oscillation period with L is compatible with the above analysis. The typical amplitude of the Pc4 pulsations varies within 5–20 nT while the Pc3 amplitude is smaller than 10 nT.

Other kind of the damped-type oscillations is shown in Fig. 6.9 (Glassmeier 1995). The H-component of the geomagnetic variations caused by a magnetospheric substorm is displayed at the upper panel. The sharp decrease of the magnetic field at

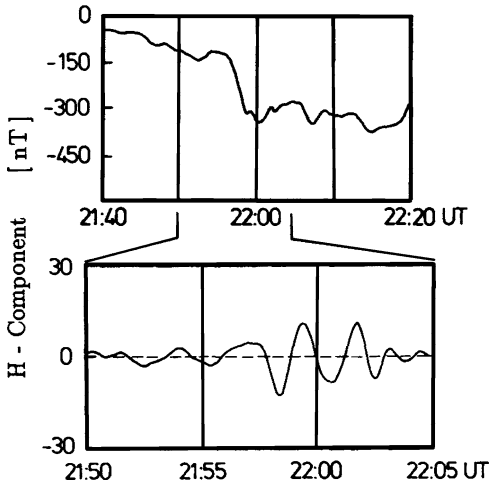

Fig. 6.9 An example of magnetic field variations during an isolated magnetospheric substorm (*upper panel*) and a Pi2 pulsation (*bottom panel*). The data displayed in the *bottom panel* are high pass filtered time series of the upper record. Taken from Glassmeier (1995)

21:57 UT is an evident signature of the substorm onset. The data at the bottom panel is high pass filtered to yield a magnetogram of the Pi2 pulsation with period about 150 s and amplitude about 10 nT. The trains of Pi2 pulsations are usually observed at the nightside of the Earth. Their amplitude about 1–50nT tends to maximize in the vicinity of aurora region at midnight.

The long-period pulsation trains, such as Pc3, Pc4, Pc5, and Pi2 pulsations, are believed to be due to eigenoscillations of the Earth magnetosphere (Kato 1962; Zibyn and Yu 1965). The Alfvén oscillations can explain the basic properties of the Pc5 pulsations and, in some cases, the patterns of the Pc4 pulsations. The observed dependence of pulsation period on the latitude is consistent with that predicted by the FLR theory we have treated in the previous sections (Guglielmi and Troitskaya 1973). Likewise, a number of pulsation events exhibit a rather localized wavefield of extension 100–200 km in north–south direction and about 500–1,000 km in east–west direction (Glassmeier 1980). The additional argument that is in favor of the resonance origin of the Pc4, Pc5 pulsations is that these pulsations are well correlated at the magneto-conjugate points (Guglielmi and Troitskaya 1973). Lanzerotti and Fukunishi (1974) have found that in the ground magnetic observation the odd mode of the Alfvén oscillations is prevailed so that the amplitude of the oscillation reaches a peak value at the equator. On the other hand the amplitude of these pulsations grows with increase of the latitude (Ziesolleck et al. 1993). This suggests that the source of the pulsations is at the periphery of the magnetosphere. The fundamental mode of the FLR oscillations manifests itself through Pc5 pulsations as observed on board the satellites OGO 5 and GEOS 2 (Singer and Kivelson 1979; Junginger et al. 1984). A signature of the fundamental

mode together with higher harmonic of the same field-line shell has been detected by Singer et al. (1979), Baumjohann and Glassmeier (1984) and Engebretson et al. (1986).

A detailed review of observations of the ULF pulsation is outside the scope of this section, and the interested reader is referred to the excellent tutorial review by Glassmeier (1995) for detail about the horizontal polarization, wave propagation across the ambient magnetic field and other properties of the ULF fields.

Only a few observations may have interpreted as global poloidal eigenoscillations that may be associated with the cavity mode (Higbie et al. 1982; Kivelson et al. 1984). An observational hint toward the existence of cavity mode has been reported by Crowley et al. (1987) on the basis of measurements of the ionospheric Pedersen conductivity and damping rates of the ULF pulsations

The short-period pulsations such as Pi1, Pc1, Pc2 contain a wide variety of shape compared to the long-period pulsations. To describe this diversity of the short-period pulsations, we use the additional nomenclature including "pearl-type micropulsations," "interval of pulsations of diminishing periods" (IPDP), "hydromagnetic whistler," "pulsation burst" (Guglielmi and Troitskaya 1973), "continuous emissions", and so on. A typical amplitude of the short-period pulsations is smaller than 1 nT, and these pulsations cover the frequency range from 0.025 to 5 Hz. It is generally believed that the main excitation of the short-period pulsations is due to kinetic plasma instabilities (Trakhtengerts and Rycroft 2008) resulted in the generation of MHD and ion-cyclotron waves in the frequency range of Pi1, Pc1, and Pc2.

6.3.2 *Kelvin–Helmholtz Instability at the Magnetopause*

The most prominent mechanism for Pc5 pulsations is thought to be the Kelvin–Helmholtz instability at the Earth's magnetopause (Dungey 1954). This effect is believed to be due to surface waves propagating at the flanks of the magnetopause. The surface wave may be in turn excited due to the interaction between the solar wind and the planetary magnetic field as illustrated in Fig. 6.4 (Atkinson and Watanabe 1966; Kivelson and Southwood 1985). This kind of instability may arise in a fluid flow at the boundary between two regions which are separated by a tangential discontinuity of the fluid velocity. This means that the fluid flow velocities are both parallel to the boundary and have a jump across the boundary whereas the fluid pressure is kept continuous. Consider a small random variation of the equilibrium position of the boundary. This variation, shown in Fig. 6.10 with a bulge of the boundary surface, results in restriction of the effective cross section of the flow in the upper region. From the principle of the fluid flux conversation it follows that the fluid velocity V must increase in this region. According to Bernoulli's law for an inviscid fluid

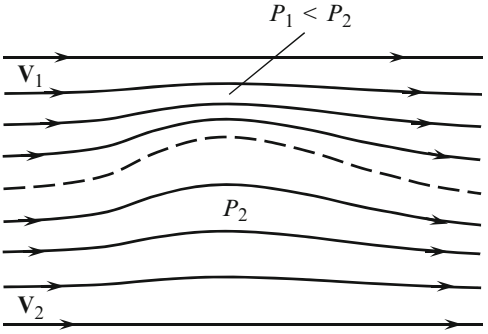

Fig. 6.10 A schematic illustration of the mechanism of Kelvin–Helmholtz instability in an inviscid fluid. The tangential discontinuity of a fluid flow is shown with *dotted line*. $\mathbf{V}_1$ and $\mathbf{V}_2$ denote the unperturbed velocities of the fluid flow on both sides of the tangential discontinuity. The fluid pressure, P_1, just over the bulge of the boundary is smaller than that under the bulge

$$\frac{\rho V^2}{2} + P = \text{const}, \tag{6.57}$$

a flow velocity increase is accompanied by the fluid pressure decrease over the bulge shown in Fig. 6.10. The pressure difference between two regions leads to further enhancement of the instability and the initial perturbation of the boundary position that result in the generation of surface waves.

In familiar hydrodynamics the tangential discontinuities are always unstable with respect to small perturbations that result in their fast turbulization. Magnetic field stabilizes the flow of conducting fluid in such a way that the tangential discontinuities in the fluid may be stable. This is due to the fact that the fluid velocity perturbations across the ambient magnetic field give rise to extension of the field lines frozen in the conducting fluid that in turn results in the generation of forces aiming to restore the unperturbed fluid flow.

The condition of instability of the tangential discontinuity in a conducting fluid/plasma is the following (e.g., see the text by Landau and Lifshitz 1982 for details)

$$\frac{B_1^2 + B_2^2}{\mu_0} < \frac{\rho_1 \rho_2}{\rho_1 + \rho_2} (V_1 - V_2)^2 , \tag{6.58}$$

where B_1 and B_2 are magnetic fields on both sides of the boundary, ρ_1 and ρ_2 are the corresponding fluid/plasma densities, and $V_1 - V_2$ stands for the relative flow velocity.

This equation can be applied to the Kelvin–Helmholtz instability arising in the magnetospheric plasma at the magnetopause. In such a case ρ_1, V_1, and B_1 may denote the plasma and field parameters of solar wind in the magnetosheath while the same values with inferior index 2 describe the magnetospheric plasma. To estimate

this effect we suppose that $\rho_1 \approx \rho_2$, and $B_1 \approx B_2$. On account of the relation $V_1 \gg V_2$ we also assume that there are no plasma motion in the magnetosphere, i.e., $V_2 \approx 0$. Substituting these values into Eq. (6.58) yields

$$V_1 > 4V_A. \tag{6.59}$$

The implication here is that if only the plasma flow in the magnetosheath is super-Alfvénic, then the Kelvin–Helmholtz instability can develop. As alluded to earlier in Sect. 1.2, the solar wind is supersonic near the Earth orbit. Across the bow shock shown in Fig. 1.8, the solar wind density and temperature increase abruptly whereas the wind velocity decreases, allowing for the presence of subsonic flow around the Earth magnetosphere. In other words, in the vicinity of local magnetic noon the solar wind flow stalls and becomes sub-Alfvénic. Toward the flanks of the magnetosphere the stream accelerates in a such way that the flow velocity becomes super-Alfvénic again. This implies that the Kelvin–Helmholtz instability may occur at the flanks of the magnetosphere, i. e., around dusk and dawn.

A number of experimental data is consistent with the solar-wind-related mechanism for excitation of the Kelvin–Helmholtz instability followed by the long-period ULF pulsations (e. g., see the text by Glassmeier 1995). First, it is usually the case that the Pc5 pulsations are observed at the flanks of the magnetosphere, especially at the downside, that are in favor of the mechanism of the Kelvin–Helmholtz instability. Moreover, analysis of the observation shows that the vector of the phase wave velocity is directed toward the tail of the magnetosphere. Second, the ULF pulsation activity and polarization characteristics are clearly controlled by the solar wind.

As discussed above, the instability of the tangential discontinuity may result in the turbulization of plasma flow followed by generation of a rather broad spectrum of perturbations. This mechanism is capable of exciting different FLRs, which may therefore form a continuous spectrum of the resonant field. This conclusion contradicts with the observations since there usually occurs only one resonance. To explain this contradiction Kivelson and Southwood (1985) have suggested that the Kelvin–Helmholtz instability caused by surface waves first results in excitation of the fundamental and higher harmonics cavity modes, that is the global poloidal eigenoscillations of the magnetosphere. As has already been stated, the spectrum of cavity modes is discrete. When these modes are excited they produce a frequency filter for wideband spectrum of the initial perturbations. At this point the FLRs can be excited by virtue of the shear Alfvén mode coupling to the resonant cavity modes. In other words, the energy of unstable surface waves may transform into the energy of poloidal oscillations which in turn can propagate across field lines up to the resonance magnetic shell thereby producing the FLR due to the mode coupling.

6.3.3 Magnetospheric Plasma Instabilities

Instabilities of the internal magnetospheric plasma distributions can be another mechanism for generation of the ULF pulsations. For one example, consider now kinetic instabilities which result in the generation of MHD and ion-cyclotron waves in the frequency range of Pc1, Pc2, and Pi1 pulsations. In a linear approximation the ion-cyclotron instability arises from the energy exchange between the wave field and charged particles. This interaction becomes the most effective under the resonance condition (e.g., see the texts by Ginzburg (1970), and Trakhtengerts and Rycroft (2008) for detail)

$$\omega - k_z V_z = n\Omega_i, \tag{6.60}$$

where ω is the wave frequency, V_z is projection of the thermal velocity of particles on ambient magnetic field, k_z is the same projection of wave vector, Ω_i is gyrofrequency of the ions, and n is integer, that is $n = 0, \pm 1, \pm 2, \ldots$ The kinematic meaning of this condition can be understood in a local reference frame fixed at the Larmor center of the particle. In this reference frame the wave frequency $\omega' = \omega - k_z V_z$ either equals zero ($n = 0$) or a multiple of the ion gyrofrequency ($n \neq 0$). Depending on the plasma particle distribution of the velocities the interaction between the MHD wave and the resonant particles may result in either enhancement or damping of the magnitude of oscillation.

This kind of the plasma instability can be due to the energetic protons ($\sim$ 10–100 keV) of the ring current region ($L \sim$ 3–6) because of anisotropy of the proton distributions with respect to the proton velocities (Cornwall 1965). The kinetic energy of the plasma particles trapped in the ring current region can thus serve as a source for energy transfer towards the ULF pulsations due to either ion-cyclotron instability mechanism or collisionless Landau damping. Notice that despite small concentration the helium ions present in plasma of the radiation ring may greatly affect the ion-cyclotron instability in the frequency range of Pc1 (Dowden 1966).

The particle bounce motion between the mirror points above the northern and southern ionospheres may cause the resonance interaction between the bounce motion and the MHD waves. The bounce motion is accompanied by large-scale drift of the plasma particles approximately perpendicular to the Earth magnetic field lines. This drift caused by the gradient and curvature of the Earth magnetic field take the particles entirely around the Earth as shown in Fig. 1.10. The MHD wave field can resonate with the bounce and drift plasma motions as the wave frequency is related to the bounce and drift frequencies through special resonance condition (Karpman et al. 1977; Southwood 1980). Moreover, the deviation of the particle distribution function from the equilibrium function is necessary to provide the drift-bounce instability. It is believed that this mechanism is capable of explaining the origin of small-scale (wave number $m \sim$ 50–100) azimuthal poloidal Pc4 pulsations and giant pulsations Pg (Takahashi 1988).

Available candidates for a source of the ULF pulsations are the so-called firehose and drift mirror plasma instabilities, which are driven by anisotropies of the plasma pressure. We cannot come close to exploring these topics in any detail, but the interested reader is referred to the text by Glassmeier (1995) for a more complete treatise on magnetospheric plasma instabilities.

6.3.4 MHD Waves Propagating in Solar Wind

An indirect hint toward the existence of a variety of MHD waves, which can propagate in the solar wind, has been provided by numerous observations and has been supported by a number of theoretical studies (e.g., Kwok and Lee 1984; Takahashi et al. 1984; Yumoto 1984; Engebretson et al. 1987). A wide variety of the solar-wind-generated waves cover a wideband frequency range including ULF pulsations region. It appears that such waves can cross the Earth's bow shock, magnetosheath, magnetopause and then penetrate deep into the magnetosphere and plasmasphere. There may also be an indirect way for the energy transfer from the interplanetary space to the magnetosphere. For example, the Alfvén and FMS wave energy can be transferred into the particle kinetic energy and back to the wave energy via ionospheric interactions.

6.3.5 Reconstruction of the Magnetospheric Configuration

All the excitation mechanisms alluded to above share a common trait since they are generated from the different kinds of plasma instabilities that can arise inside the magnetosphere, at the magnetopause, or outside the magnetosphere in the solar wind. In some sense, these mechanisms can serve as more or less permanent sources of the ULF pulsations. In the next subsection we consider more impulsive sources such as SSC and magnetic storm associated Pc5 pulsations and fast transients. The SSC is due to the sudden changes of the solar wind flow followed by variations of the dynamic pressure from the solar wind on the Earth's magnetosphere, that in turn may be sufficient in order to change position of the dayside magnetopause. The large-scale reconstruction of the magnetopause and the whole magnetosphere results in the generation of ULF pulsations, which is believed to be almost axisymmetric. The azimuthal wave numbers m associated with these pulsations seem to be close to zero. This means that both main modes of the magnetospheric eigenoscillations, i.e., toroidal and poloidal modes, can propagate through the magnetosphere independently of each other. It appears that a number of ULF pulsations are related to magnetospheric substorms in the magnetotail (Baumjohann and Glassmeier 1984).

6.4 ULF Electromagnetic Noises

6.4.1 Main Sources of the ULF Noises

The global electromagnetic resonances which have been considered in this section, cover a wide frequency range from several mHz to 30–35 Hz. The first Schumann resonances cover the overall range from 7–8 to 30–35 Hz, which are in the ELF frequency band. The IAR eigenfrequencies lie in the range from 0.5–0.25 to 3–5 Hz. The FLRs and the cavity mode eigenfrequencies are below this range since they typically cover the interval 10^{-2}–10^{-3} Hz. In what follows we focus on the natural ULF noise, that is at the frequencies which are even smaller than above resonant frequencies covering the range of the global electromagnetic resonances.

The Earth electromagnetic field is subject to a variety of random forces such as the variations of solar radiations, incident MHD waves and global magnetospheric resonances, fluctuation of the ionospheric currents, changes in the world thunderstorm activity, and so on. A variety of magnetospheric MHD waves acting on the Earth ionosphere give rise to a wideband spectrum of electromagnetic perturbations, which can be detected on the ground surface. Throughout the frequency range from HF to ULF the flux density of natural magnetic variations increase with a decrease in frequency in such a way that the amplitude of the spectral density varies from 10^{-21}–10^{-24} W/(m^2 Hz) at frequency 10^9–10^{10} Hz up to 10^{-3}–10^{-1} W/(m^2 Hz) at frequency $\sim 10^{-3}$ Hz (Lanzerotti 1978). Figure 6.11 taken from Lanzerotti et al. (1990) shows spectra of background magnetic variations measured in the wideband frequency range, which cover the ten-decades from 10^{-5} to 10^5 Hz. Interestingly enough the noise in the ELF/VLF range is an overall approximate inverse relation between the noise amplitude and frequency (Lanzerotti et al. 1990; Fraser-Smith 1995). This implies that there is an overall approximate inverse relation between the noise power amplitude and frequency. Notice that a power law spectrum of noise, which is referred to as the class of $1/f$ noise, or flicker noise, is usually observed in all electric devices over a very broad frequency range (e.g., see Rytov et al. 1978; Weissman 1988). There exists other tendency in the frequency range from 10^{-5} to 10^{-1} Hz where in the first approximation the noise amplitude is inversely proportional to $f^{-1.5}$. As indicated in Fig. 6.11, the spectrum of the noise amplitude in the intermediate interval can be approximated by a power law proportional to f^{-n} with the exponent n laying in the range 1.0–1.5. However, the value of n appears to vary considerably, depending on the case study, measurement technique and on the instruments arranged at the ground-recording station.

Knowledge of these tendencies for the natural low-frequency noise is of special interest in geophysical studies, since it gives information about spatiotemporal variations of the natural ULF electromagnetic noise and their source mechanism. This knowledge is also important from a scientific point of view, because, as pointed out by Fraser-Smith (1995), it is not understood at present why there exists such a relation between the ULF noise amplitude and frequency.

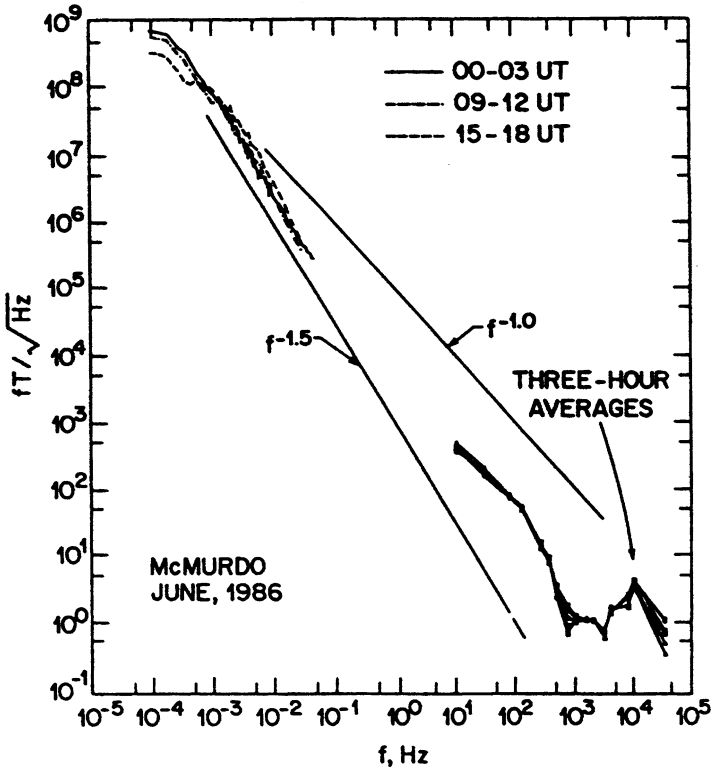

Fig. 6.11 Measured monthly average 3-h power spectra for magnetic field variations. The data were gathered at Arrival Heights, Antarctica near McMurdo Station, during June 1986. Taken from Lanzerotti et al. (1990)

To a certain extent the sources of the natural ULF variations can be divided into two general classes, depending on whether they are external or internal to the magnetosphere. It is now generally accepted that the external sources are mainly due to the interaction of the Earth's magnetosphere with solar wind and with MHD waves coming from outer space. Under certain orientation of the interplanetary magnetic field (IMF) and the Earth's magnetic field lines, when partial reconnection of the field lines occurs, the small quasiperiodic variations of the IMF ($\sim$ 10 nT) may result in generation of the ground-based variations with amplitude of about several hundred Tesla (Pilipenko et al. 2000). The energy of turbulent noise generated in the magnetosheath can penetrate through the magnetopause and thus can get trapped in the magnetosphere thereby exciting ULF noise and MHD waves.

An important example of internal sources is the global lightning activity, considering that there is about 2×10^3 thunderstorm in progress around the world at any time.

The sources of natural ULF noise covering the frequency range 10^{-4}–10^{-2} Hz have not yet been adequately explored. It is customary to conjecture that the MHD waves traveling through the magnetosphere can transfer a variety of electromagnetic noises from the outer regions of the magnetosphere towards the Earth. The high frequency region of the noise spectrum is lost in the conducting E layer of the ionosphere. In this picture the E layer plays a major role in formation of the ULF noise in the neutral atmosphere. Furthermore, the ionospheric current variations due to fluctuations of the ionospheric plasma conductivity and of neutral wind velocity can produce an additional random perturbation in the ULF region.

6.4.2 Model and Basic Equations

In what follows we focus our attention on the two possible sources, which are the incident MHD waves and the ionospheric current fluctuations originated from variation of the neutral gas flow in the altitude range of the ionospheric E layer. The field fluctuations in the magnetosphere and ionosphere can excite a random electromagnetic field in the atmosphere and on the ground surface. At first we consider the fields of the MHD wave and of the wind-driven currents in the ionosphere as given deterministic functions, which play a role of forcing functions. Solving this problem we can find the transfer matrices, which relate the fields in the ionosphere and magnetosphere with the fields in neutral atmosphere. Since the characteristic spatial size of the ULF variations is supposed to be smaller than the Earth radius, the curvature of the magnetic field lines is disregarded. This implies that the undisturbed geomagnetic field is considered as a homogeneous one.

To approximate the actual variation of medium parameters with altitude, we consider a plane-stratified medium model, which consists of the magnetosphere, conducting ionosphere, neutral atmosphere and conducting earth, as shown in Fig. 6.12. Consider first the conducting E layer of the ionosphere. We use a traditional coordinate system in which the y axis is directed westward, the x axis to the north, and z axis vertically upward. The origin of the local coordinate system is situated on the boundary between the bottom of the ionosphere and the neutral atmosphere. The vector of the Earth magnetic field is situated at the meridional x, z plane and makes an angle γ with respect to the horizontal axis x. The inclination angle is chosen in such a way that γ is positive for the northern hemisphere.

Let $\delta\mathbf{B}$ be a small perturbation of the geomagnetic field $\mathbf{B}_0$, i.e., $\delta B \ll B_0$. In the frequency range of interest the conduction current is much greater than the displacement one so the Ampere's law (1.5) holds at the E-layer. The Ohm's law for the ionospheric plasma of the E-layer is given by Eq. (2.6). Combining these equations we get

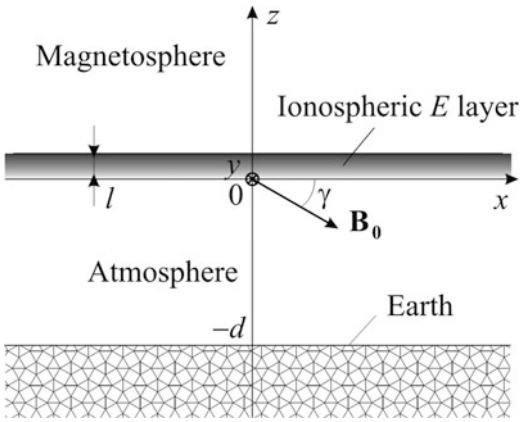

Fig. 6.12 Schematic illustration of a stratified medium model

$$\partial_y \delta B_z - \partial_z \delta B_y = \mu_0 \left\{ \sigma_\parallel E_\parallel \cos\gamma + J_\perp \sin\gamma + J_x^{(w)} \right\}, \tag{6.61}$$

$$\partial_z \delta B_x - \partial_x \delta B_z = \mu_0 \left\{ \sigma_P E_y - \sigma_H \left(E_x \sin\gamma + E_z \cos\gamma \right) + J_y^{(w)} \right\}, \tag{6.62}$$

$$\partial_x \delta B_y - \partial_y \delta B_x = \mu_0 \left\{ -\sigma_\parallel E_\parallel \sin\gamma + J_\perp \cos\gamma + J_z^{(w)} \right\}, \tag{6.63}$$

where as before $\sigma_\parallel$ denotes the field-aligned plasma conductivity, σ_H and σ_P are the Hall and Pedersen conductivities. Here we made use of the following abbreviations:

$$E_\parallel = E_x \cos\gamma - E_z \sin\gamma, \tag{6.64}$$

$$J_\perp = \sigma_P \left(E_x \sin\gamma + E_z \cos\gamma \right) + \sigma_H E_y. \tag{6.65}$$

The wind-driven current density is given by

$$\begin{aligned} J_x^{(w)} &= B_0 \left(\sigma_H V_\perp - \sigma_P V_y \right) \sin\gamma, \quad J_z^{(w)} = J_x^{(w)} \cot\gamma, \\ J_y^{(w)} &= B_0 \left(\sigma_H V_\perp + \sigma_P V_y \right), \end{aligned} \tag{6.66}$$

where V_x, V_y and V_z are the component of the mass velocity of the neutral wind, and $V_\perp = V_x \sin\gamma + V_z \cos\gamma$. Notice that the neutral gas dominates below 130 km in such a way that the charged particles cannot greatly affect the neutral gas flow. This implies that the mass gas velocity can be considered as a given/forcing function which affects the electromagnetic fields and conduction currents inside the conducting E layer of the ionosphere. Furthermore, the parallel plasma conductivity in this region is much greater than the Hall and Pedersen ones. Assuming that $\sigma_\parallel \to \infty$, the parallel electric field $\mathbf{E}_\parallel$ thus becomes zero, i.e.,

$$E_z \sin\gamma = E_x \cos\gamma. \tag{6.67}$$

In order to eliminate the nonzero parallel current $\sigma_{\parallel} E_{\parallel}$ from Eqs. (6.61) and (6.63) one should slightly rearrange these equations. Equation (6.61) multiplied by $\sin\gamma$ plus equation (6.63) multiplied by $\cos\gamma$ gives

$$\left(\partial_y \delta B_z - \partial_z \delta B_y\right)\sin\gamma + \left(\partial_x \delta B_y - \partial_y \delta B_x\right)\cos\gamma = \mu_0\left(J_{\perp} + J_x^{(w)}\sin\gamma + J_z^{(w)}\cos\gamma\right). \tag{6.68}$$

In the frequency range $f < 0.1$ Hz the thickness, l, of the E layer is much smaller than the skin-depth in the ionosphere. In this notation the "thin" layer approximation can be used in order to derive the boundary conditions at the E layer of the ionosphere. This approximation is described in more detail in Sect. 5. Integrating of Eq. (6.68) with respect to z across the E-layer, making formally $l \to 0$, and taking into account Eq. (6.67), gives the boundary conditions at $z = 0$

$$-\sin\gamma\left[\delta B_y\right] = \mu_0\left(\Sigma_P E_x/\sin\gamma + \Sigma_H E_y + I^{(w)}\right), \tag{6.69}$$

where the square brackets denote the jump of magnetic field across the E-layer, Σ_P and Σ_H are the height-integrated Pedersen and Hall conductivities given by Eq. (5.25). Here $I^{(w)} = I_x^{(w)}\sin\gamma + I_z^{(w)}\cos\gamma$ stands for the height-integrated wind-driven currents, i.e.

$$I_x^{(w)} = \int_0^l J_x^{(w)} dz \quad \text{and} \quad I_z^{(w)} = \int_0^l J_z^{(w)} dz. \tag{6.70}$$

Similarly, integrating of Eq. (6.62) with respect to z across the E-layer yields

$$\left[\delta B_x\right] = \mu_0\left(\Sigma_P E_y - \Sigma_H E_x/\sin\gamma + I_y^{(w)}\right), \tag{6.71}$$

where $I_y^{(w)}$ is another component of the height-integrated wind-driven current, i.e.

$$I_y^{(w)} = \int_0^l J_y^{(w)} dz. \tag{6.72}$$

In the framework of our model the region above the E-layer is supposed to be the area consisting solely of a cold collisionless plasma, which is described by Eq. (5.2). In the ULF frequency range the absolute value of parallel components of the plasma dielectric permittivity, $\varepsilon_{\parallel}$, is much greater than perpendicular ones and thus can be assumed to be infinite. This means that the parallel electric field $\mathbf{E}_{\parallel}$ equals approximately zero, and we come to Eq. (6.67). Thus, we can eliminate the parallel current from Eq. (5.2) in analogy to the procedure used for the derivation of Eq. (6.68). Whence, we get

$$\left(\partial_y \delta B_z - \partial_z \delta B_y\right) \sin\gamma + \left(\partial_x \delta B_y - \partial_y \delta B_x\right) \cos\gamma = -\frac{i\omega}{V_A^2} \left(E_x \sin\gamma + E_z \cos\gamma\right), \tag{6.73}$$

$$\partial_z \delta B_x - \partial_x \delta B_z = -\frac{i\omega}{V_A^2} E_y, \tag{6.74}$$

where $V_A = c/\varepsilon_\perp^{1/2}$ is the Alfvén velocity. These equations should be supplemented by the Faraday's law given by Eq. (4.2), where $\mathbf{B}$ should be replaced by $\delta\mathbf{B}$. The neutral atmosphere ($-d < z < 0$) is considered as an insulator, and the solid Earth ($z < -d$) as a uniform conductor with a constant conductivity σ_g. If the displacement current in both media is disregarded, the electromagnetic perturbations are described by Eqs. (5.27) and (5.28).

6.4.3 Transfer Matrices

Solution of the above problem with proper boundary conditions relates the magnetic perturbations on the ground surface with the forcing functions, i.e., the amplitudes of the MHD waves and of the wind-driven ionospheric current. We seek for the solution of the problem in the form of spatiotemporal Fourier transform. This implies that all quantities vary as $\exp(i\mathbf{k}\cdot\mathbf{R} - i\omega t)$, where $\mathbf{k}$ is horizontal wave vector, and $\mathbf{R} = (x, y)$. Let $\delta\mathbf{b}(\mathbf{k}, \omega, z)$ and $\delta\mathbf{e}(\mathbf{k}, \omega, z)$ be Fourier transforms of the magnetic and electric field variations, respectively. Let $\delta\mathbf{b}^{(m)}(\mathbf{k}, \omega)$ be the spectral amplitude of the incident Alfvén and FMS waves in the ionosphere, while $\delta\mathbf{I}^{(w)}(\mathbf{k}, \omega)$ stands for the height-integrated wind-driven ionospheric current. This latter value denotes a Fourier transform of the functions $I_x^{(w)}$, $I_y^{(w)}$ and $I_z^{(w)}$ given by Eqs. (6.70) and (6.72), respectively. In consequence of linearity of both Maxwell equations and boundary conditions, the spectral densities of the ionospheric and atmospheric fields are coupled in a linear fashion through the transfer matrices $\hat{\mathbf{M}}^{(w)}(\mathbf{k}, \omega, z)$ and $\hat{\mathbf{M}}^{(m)}(\mathbf{k}, \omega, z)$

$$\delta\mathbf{b}(\mathbf{k}, \omega, z) = \hat{\mathbf{M}}^{(w)}(\mathbf{k}, \omega, z) \cdot \delta\mathbf{I}^{(w)}(\mathbf{k}, \omega) + \hat{\mathbf{M}}^{(m)}(\mathbf{k}, \omega, z) \cdot \delta\mathbf{b}^{(m)}(\mathbf{k}, \omega). \tag{6.75}$$

We now omit the detailed derivation of the transfer matrices. The interested reader is referred to the paper by Surkov and Hayakawa (2007, 2008) for details. If the vertical ambient magnetic field is assumed then an analytical solution of the problem can be found for arbitrary value of $\mathbf{k}$. As the magnetic field $\mathbf{B}_0$ is vertically downward one should therefore substitute $\gamma = \pi/2$ in the basic equations. In such a case the set of Eqs. (6.73), (6.74), and (4.2) can be split into two independent sets, which describe the shear Alfvén and FMS waves propagating in the magnetospheric plasma. Similarly, the set of Eqs. (5.27) and (5.28) for the atmosphere and the ground can be split into two independent sets, which describe the TM and TE modes in the atmosphere. These two modes are coupled through boundary conditions at

the ionosphere, that is via Eqs. (6.69), (6.71) and via the continuity condition for $\delta\mathbf{b}$ and for the horizontal components of $\delta\mathbf{e}$. In this notation the wavefield of the incident Alfvén and FMS waves in the magnetosphere is assumed to be given functions whereas the waves reflected from the ionosphere should be found to fit the solutions in the magnetosphere and the atmosphere. Considering the large-scale perturbations with the scale size $2\pi/k \sim 10^3$ km, we restrict our analysis on an extreme case of $\omega \ll kV_A \approx 30$ Hz ($f = \omega/2\pi \ll 5$ Hz) and even on the case of stronger inequality $\omega \ll k_x^2/\left(\mu_0\sigma_g\right) \approx 0.03$ Hz ($f \ll 0.005$ Hz). In such a case the matrix $\hat{\mathbf{M}}^{(w)}$ for the ground surface $z = -d$ can be simplified to

$$\hat{\mathbf{M}}^{(w)} \approx \frac{i\mu_0 \exp(-kd)}{2g_3} \begin{pmatrix} ik_x f_-/k & ik_x f_+/k & 0 \\ ik_y f_-/k & ik_y f_+/k & 0 \\ f_- & f_+ & 0 \end{pmatrix}, \tag{6.76}$$

where $g_3 = 1 + \alpha_P$. Here we made use of the following abbreviations:

$$f_+ = \frac{k_y\alpha_H + k_x g_3}{k}, \quad f_- = \frac{k_x\alpha_H - k_y g_3}{k},. \tag{6.77}$$

The third column in the matrix consists of zeros because the wind velocity component parallel to the vertical magnetic field $\mathbf{B}_0$ cannot excite the magnetic perturbations. The similar expression for matrix $\hat{\mathbf{M}}^{(m)}$ can be found in the paper by Surkov and Hayakawa (2008).

Furthermore, the study is simplified if the components of the horizontal wave vector satisfy the requirement $k_x \gg k_y$. This implies that the azimuthal scale size of the perturbations is much greater than that of the meridional perturbations. In fact, we assume a 1D distribution of the height-integrated ionospheric current, $\delta\mathbf{I}^{(w)}(x,t)$, as a source of 2D random electromagnetic fields in the surroundings. The east–west neutral winds at the altitude range of the E layer can excite the ring current in the ionosphere thereby producing this type of perturbations. For one more example, it is worth mentioning that the Pc5 pulsations have a rather localized wavefield of extension 100–200 km in north–south direction.

On the basis of this simplifying assumption, the analytic form of the transfer matrices can be simplified. Considering the large-scale perturbations the matrix $\hat{\mathbf{M}}^{(w)}$ at $z = -d$ is given by

$$\hat{\mathbf{M}}^{(w)} \approx \frac{i\mu_0 \exp(-kd)}{2g_2} \begin{pmatrix} i\alpha_H \sin\gamma & ig_2 & i\alpha_H \cos\gamma \\ 0 & 0 & 0 \\ k\alpha_H \sin\gamma/k_x & kg_2/k_x & k\alpha_H \cos\gamma/k_x \end{pmatrix}, \tag{6.78}$$

where $g_2 = \alpha_P + \sin\gamma$. The TM mode in the atmosphere contains the components δb_y, δe_x, and δe_z that are identical with those of the shear Alfvén wave in the magnetosphere. Both these modes ares coupled by virtue of boundary conditions

at $z = 0$. The second strings in the matrices consist of zeros because $\delta b_y = 0$ everywhere under the ionosphere including at $z = -d$. This means that the magnetic field due to Alfvén mode cannot penetrate through the conducting ionosphere to generate the magnetic perturbations in the atmosphere on the ground surface. So, in this model only the TE mode which includes the components δb_x, δb_z, and δe_y can contribute to the magnetic variation in the atmosphere.

As is seen from these two expressions for $\hat{\mathbf{M}}^{(w)}$, the propagation of the ULF perturbations through the conducting ionosphere and the neutral atmosphere towards the ground is accompanied by the wavefield damping with the exponential factor $\exp(-kd)$. It should be noted that in the low-frequency limit the transfer matrix is not a function of frequency. One may suppose that these conclusions hold not only for the cases examined above but also for an arbitrary angle γ and wave vector $\mathbf{k}$.

6.4.4 Correlation Matrix of Random Fields

In this section the MHD waves propagating from the magnetosphere towards the ionosphere and the ionospheric wind-driven currents are treated as the random functions of coordinate and time. Let $\delta\mathbf{B}(\mathbf{r}, t)$ and $\delta\mathbf{E}(\mathbf{r}, t)$ be the random electromagnetic variations at the point $\mathbf{r} = (x, y, z)$ produced by the fluctuations of the random electromagnetic fields in the ionosphere. In practice, the mean value of the random magnetic variations is close to zero. Therefore, we will be interested in the correlation matrix/product moment, which has the form

$$\Psi_{nm}^{(B)}\left(\mathbf{r}, t, \mathbf{r}', t'\right) = \left\langle \delta B_n(\mathbf{r}, t)\, \delta B_m^*\left(\mathbf{r}', t'\right)\right\rangle, \tag{6.79}$$

where the brackets $\langle\rangle$ denotes the averaging over all available realizations of the random process, the symbol $*$ denotes a complex-conjugate value and the inferior indexes n and m are taken on the values x, y, and z. This correlation matrix describes the spatial and temporal correlation of the field components $\delta B_n(\mathbf{r}, t)$ and $\delta B_m^*(\mathbf{r}', t')$ taken at different points $\mathbf{r}$ and $\mathbf{r}'$, and at different time t and t'.

In a similar fashion we may introduce the correlation matrix, $\Psi_{nm}^{(E)}$, of the electric field fluctuations. Notice that Eq. (6.79) satisfies both real and complex random fields. In a similar fashion we may introduce the correlation matrix of the forcing function fluctuations, $\Psi_{nm}^{(m)}$ and $\Psi_{nm}^{(w)}$.

It is clear that the spectral amplitudes of the forcing functions, $\delta\mathbf{b}^{(m)}(\omega, \mathbf{k})$ and $\delta\mathbf{I}^{(w)}(\omega, \mathbf{k})$, and of the magnetic, $\delta\mathbf{b}(\mathbf{k}, \omega, z)$, and electric, $\delta\mathbf{e}(\mathbf{k}, \omega, z)$, field fluctuations are random functions as well. By contrast, the transfer matrices are considered to be deterministic/given functions. The spectra of random electromagnetic fluctuations on the ground surface are related to the spectral amplitudes, $\delta\mathbf{b}^{(m)}(\omega, \mathbf{k})$ and $\delta\mathbf{I}^{(w)}(\omega, \mathbf{k})$, through the linear equation (6.75).

Considering the ground-based observation we first study the spectral density of correlation matrix of the magnetic perturbations given by

$$\psi_{nm}^{(B)}\left(\omega,\mathbf{k},\omega',\mathbf{k}'\right)=\left\langle \delta b_n\left(\omega,\mathbf{k}\right)\delta b_m^*\left(\omega',\mathbf{k}'\right)\right\rangle, \tag{6.80}$$

where the symbols in the brackets denote the spectral amplitudes of the ground-based field fluctuations.

Substituting Eq. (6.75) for $\delta\mathbf{b}$ into Eq. (6.80) and rearranging yields

$$\psi_{nm}^{(B)}=\sum_{l=1}^{3}\sum_{p=1}^{3}\left(\hat{M}_{nl}^{(w)}\hat{M}_{mp}^{(w)*}\psi_{lp}^{(w)}+\hat{M}_{nl}^{(m)}\hat{M}_{mp}^{(m)*}\psi_{lp}^{(m)}\right), \tag{6.81}$$

where

$$\psi_{lp}^{(w)}=\left\langle \delta I_l^{(w)}\left(\omega,\mathbf{k}\right)\delta I_p^{(w)*}\left(\omega',\mathbf{k}'\right)\right\rangle, \tag{6.82}$$

$$\psi_{lp}^{(m)}=\left\langle \delta b_l^{(m)}\left(\omega,\mathbf{k}\right)\delta b_p^{(m)*}\left(\omega',\mathbf{k}'\right)\right\rangle. \tag{6.83}$$

Here we have assumed that the forcing functions, $\delta\mathbf{b}^{(m)}\left(\omega,\mathbf{k}\right)$ and $\delta\mathbf{I}^{(w)}\left(\omega,\mathbf{k}\right)$, are statistically independent of each other.

In what follows we focus on the correlation matrix, which describes the contribution of the ionospheric wind-driven currents to the natural electromagnetic noise observed on the ground surface. We choose first to study the case of vertical Earth's magnetic field. The fluctuations of height-integrated ionospheric current, $\delta\mathbf{I}^{(w)}\left(\mathbf{R},t\right)$, is considered as a 2D random field of $\mathbf{R}=(x,y)$. This random field is assumed to be uniform in time so that shift of the initial time has no effect on the random process. In this notation the spatiotemporal correlation functions, $\Psi_{lp}^{(w)}$, and their linear combination in Eq. (6.81) depend on the time difference $\tau=t-t'$. If the random field is uniform in space, the shift of the origin of coordinate system O is insignificant, so that the correlation functions must depend on only relative distance $L=|\mathbf{L}|=\left|\mathbf{R}-\mathbf{R}'\right|$. Since the plasma conductivity is anisotropic in the E layer, $\Psi_{lp}^{(w)}$ cannot depend only on relative distance. So we assume that $\Psi_{lp}^{(w)}$ is a function of both $L_x=|x-x'|$ and $L_y=|y-y'|$. In such a case the spectral density of this random process is delta-correlated both over k_x, k_y and ω

$$\psi_{lp}^{(w)}\left(\mathbf{k},\omega,\mathbf{k}',\omega'\right)=\delta\left(\omega-\omega'\right)\delta\left(k_x-k_x^{'}\right)\delta\left(k_y-k_y^{'}\right)G_{lp}\left(\omega,\mathbf{k}\right). \tag{6.84}$$

Here the function $G_{lp}\left(\omega,k\right)$ is derivable through the spatial distribution of the correlation function $\Psi_{lp}^{(w)}\left(\mathbf{L},\omega\right)$

$$G_{lp}\left(\omega,\mathbf{k}\right)=\frac{1}{4\pi^2}\int_{-\infty}^{\infty}\int_{-\infty}^{\infty}\Psi_{lp}^{(w)}\left(\mathbf{L},\omega\right)\exp\left(-i\,\mathbf{k}\cdot\mathbf{L}\right)dL_x dL_y. \tag{6.85}$$

Now we choose for study the Gaussian-shaped form of the correlation function. Since the random fields are anisotropically distributed on the ground surface, the function $\Psi_{lp}^{(w)}(\mathbf{L},\omega)$ may depend on two correlation radii, so it can be chosen in the form

$$\Psi_{lp}^{(w)}(\mathbf{L},\omega) = F_{lp}(\omega)\exp\left(-\frac{L_x^2}{\rho_x^2(\omega)} - \frac{L_y^2}{\rho_y^2(\omega)}\right). \tag{6.86}$$

The radii $\rho_x(\omega)$ and $\rho_y(\omega)$ characterize the correlations of the wind-current fluctuation in the x and y-directions, respectively. The functions $F_{lp}(\omega)$ depend on how the height-integrated current $I_l^{(w)}$ is correlated with the current $I_p^{(w)}$. In particular, if these currents are statistically independent of each other, then $F_{lp}(\omega) = 0$. In the subsequent discussion we define both the specific form of the correlation radius and the factor $F_{lp}(\omega)$.

Substituting Eq. (6.86) for $\Psi_{lp}^{(w)}$ into Eq. (6.85), performing integration over L_x and L_y, yields

$$G_{lp}(\omega,\mathbf{k}) = \frac{F_{lp}\rho_x\rho_y}{4\pi}\exp\left(-\frac{k_x^2\rho_x^2 + k_y^2\rho_y^2}{4}\right). \tag{6.87}$$

In situ measurements the horizontal magnetic field variations are greater than the vertical one. As one example, we consider now the correlation function $\Psi_{xx}^{(B)}(\mathbf{L},\omega)$. In fact, this correlation function describes the spatial correlation of the spectral components $\delta B_x(\mathbf{r},\omega)$ and $\delta B_x^*(\mathbf{r}',\omega)$ taken at different points $\mathbf{r}$ and $\mathbf{r}'$ at frequency ω. For practical purposes, it is interesting to study the spectral density/power spectrum, which is based on a single-stationed three-component magnetometer recording. If the data for the power spectra is gathered in a single point, only autocorrelation function is available. In this notation, substituting Eqs. (6.76), (6.84), (6.87) into Eq. (6.81), applying an inverse Bessel transform, and setting $\mathbf{L} = \mathbf{R} - \mathbf{R}' = 0$, yields

$$\Psi_{xx}^{(B)}(0,\omega) = \frac{\mu_0^2\rho_x\rho_y}{16\pi g_3}\int_{-\infty}^{\infty}\int_{-\infty}^{\infty}\left\{F_{xx}f_-^2 + \left(F_{xy} + F_{yx}\right)f_-f_+ + F_{yy}f_+^2\right\}$$
$$\times\exp\left(-\frac{k_x^2\rho_x^2 + k_y^2\rho_y^2}{4} - 2kd\right)\frac{k_x^2}{k^2}dk_xdk_y, \tag{6.88}$$

In the extreme case of small correlation radii, i.e., $2d \gg \rho_x, \rho_y$, one can find that

$$\Psi_{xx}^{(B)}(\omega) = \Psi_{xx}^{(B)}(0,\omega) \approx \frac{\mu_0^2\rho_x(\omega)\,\rho_y(\omega)\,\Theta(\omega)}{256d^2}, \tag{6.89}$$

where

$$\Theta(\omega) = \left(\frac{3\alpha_H^2}{g_3} + g_3\right) F_{xx}(\omega) + \left(\frac{\alpha_H^2}{g_3} + 3g_3\right) F_{yy}(\omega) + 2\alpha_H \left\{F_{xy}(\omega) + F_{yx}(\omega)\right\}. \tag{6.90}$$

Within the altitudes of the E-layer the ratio of plasma to neutrals number densities is 10^{-7}–10^{-9} for the day- and night-time conditions, respectively. This means that the motions of electrons and ions practically have no effect on the pattern of neutral has flow. In contrast, the moving neutrals drag the ions thereby exciting the wind-driven ionospheric currents. In our model we leave out of account the diurnal variations and fluctuation of the ionospheric plasma conductivity due to the variation of solar radiation and other causes. This implies that the spatiotemporal distribution of the wind-driven currents is basically governed by the hydrodynamic processes and fluctuations of the neutrals flow in the ionosphere. Such fluctuations may propagate with the velocities of acoustic and atmospheric gravity waves, which frequently occur at the altitudes of the E-layer. In this picture the correlation radius, $\rho_c(\omega)$, of the random fields can be roughly estimated as (Surkov and Hayakawa 2007)

$$\rho_c(\omega) \sim V_a(\omega)\, T = \frac{2\pi V_a(\omega)}{\omega}. \tag{6.91}$$

Here $V_a(\omega)$ denotes the acoustic wave velocity or the mass velocity of the neutrals and T stands for a typical period of ionospheric parameter variations.

Finally, using Eq. (6.91) to estimate the correlation radii, ρ_x and ρ_y, we obtain the following rough estimate of the power spectrum

$$\Psi_{xx}^{(B)}(\omega) \sim \frac{\mu_0^2 \pi^2 V_a^2(\omega)\, \Theta(\omega)}{64\omega^2 d^2}. \tag{6.92}$$

In a similar fashion we may examine the 2D field of the electromagnetic fluctuations that can be expressed via the transfer matrix (6.78). Using this line of reasoning, the spectral density of correlation matrix $\psi_{nm}^{(B)}$ is found to be given by Eq. (6.81) where the coefficients $\hat{M}_{nl}^{(w)}$ and $\hat{M}_{mp}^{(w)*}$ stand for the components of the matrix (6.81). The 1D random fields, $\delta\mathbf{I}^{(w)}(x,t)$, of the height-integrated currents is considered to be uniform in the ionosphere in such a way that the spatiotemporal correlation functions, $\Psi_{lp}^{(w)}$, and their linear combinations depend only on the time difference $\tau = t - t'$ and relative distance $\rho = |x - x'|$. As before we choose for study the Gaussian-shaped form of the correlation function of the ionospheric current fluctuations

$$\Psi_{lp}^{(w)}(\rho,\omega) = F_{lp}(\omega) \exp\left(-\frac{\rho^2}{\rho_c^2(\omega)}\right), \tag{6.93}$$

where $\rho_c\,(\omega)$ stands for the correlation radius. The spectral density of this random process is given by

$$\psi_{lp}^{(w)}\left(k_x,\omega,k_x',\omega'\right)=\delta\left(\omega-\omega'\right)\delta\left(k_x-k_x'\right)G_{lp}\left(k_x,\omega\right), \tag{6.94}$$

where δ denotes Dirac's function and

$$G_{lp}\left(k_x,\omega\right)=\frac{F_{lp}\left(\omega\right)\rho_c\left(\omega\right)}{2\pi^{1/2}}\exp\left(-\frac{k_x^2\rho_c^2\left(\omega\right)}{4}\right). \tag{6.95}$$

Combining these equations, applying an inverse Fourier transform, and performing the integration over k_x' and k_x, leads to the spatial distribution of the spectral density of the horizontal magnetic field variations. Setting $\rho=x-x'=0$ yields

$$\Psi_{xx}^{(B)}\left(\omega\right)=\frac{\mu_0^2\Theta_1\left(\omega\right)}{4}\exp\left(\frac{4d^2}{\rho_c^2\left(\omega\right)}\right)\left\{1-\mathrm{erf}\left(\frac{2d}{\rho_c\left(\omega\right)}\right)\right\}, \tag{6.96}$$

where $\mathrm{erf}\,(x)$ denotes the error function. Here the function $\Theta_1\left(\omega\right)$ is given by

$$\Theta_1\left(\omega\right)=\sum_{l=1}^{3}\sum_{p=1}^{3}\hat{m}_{xl}^{(w)}\hat{m}_{xp}^{(w)*}F_{lp}\left(\omega\right), \tag{6.97}$$

where $\hat{m}_{lp}^{(w)}$ stands for the matrix elements appearing in Eq. (6.78). When considering the extreme case $2d\gg\rho_c$, Eq. (6.96) is simplified to

$$\Psi_{xx}^{(B)}\left(\omega\right)=\frac{\mu_0^2\Theta_1\left(\omega\right)\rho_c\left(\omega\right)}{8\pi^{1/2}d}. \tag{6.98}$$

Substituting Eq. (6.91) for $\rho_c\left(\omega\right)$ into Eq. (6.98) gives the estimate of the power spectrum on the ground surface for the case of 1D distributions of the ionospheric current fluctuations

$$\Psi_{xx}^{(B)}\left(\omega\right)\sim\frac{\mu_0^2\pi^{1/2}\Theta_1\left(\omega\right)V_a\left(\omega\right)}{4\omega d}. \tag{6.99}$$

When this result is compared with Eq. (6.92), it is apparent that the 2D-case correlation function falls off more rapidly with frequency than does the 1D-case correlation function. In the analysis that follows, we show that Eq. (6.92) is better consistent in magnitude with the observations than does Eq. (6.99).

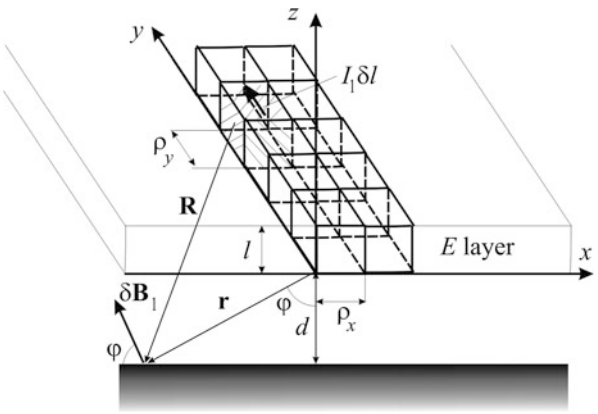

Fig. 6.13 A simplified model of random ionospheric currents that are used to gain better understanding of the solution with rigorous formulation of the problem. The current fluctuations are correlated inside each cell with sizes ρ_x and ρ_y but not correlated with respect to each other. **R** is the position vector drawn from the cell to the observation point, and $\delta\mathbf{B}_1$ is the magnetic variation caused by the current element $I_1\delta l$

6.4.5 *Rough Estimate of Spectral Density*

To gain better understanding of the results alluded to above, it is necessary to give a simple interpretation of these results on the basis of a simplified model of the medium. To be specific, we consider E region of the ionosphere as a thin isotropically conducting layer, and only the wind-driven current flowing in the y-direction is taken into account. First, we note that the fluctuations of this current can be considered as the correlated current fluctuations inside the region with horizontal sizes of the order of $\rho_x(\omega)$ and $\rho_y(\omega)$. Consider such a region as shown in Fig. 6.13 with the shaded area, as an elementary current element. The magnetic perturbations, δB_1, originated from a solitary current element on the ground surface can be estimated via Biot–Savart law

$$\delta B_1 = \frac{\mu_0 r I_1 \delta l}{4\pi \left(r^2 + y^2\right)^{3/2}}, \tag{6.100}$$

where $I_1\delta l$ denotes the current moment, $r = \left(x^2 + d^2\right)^{1/2}$ is the distance shown in Fig. 6.13, and d is thickness of the neutral atmosphere. The horizontal component is related to δB_1 through $\delta B_{1x} = \delta B_1 \cos\varphi = \delta B_1 d/r$. The effective length of the current element is estimated as follows: $\delta l \sim \rho_y$ while the current amplitude can be expressed through the height-integrated wind-driven current density, $I_y^{(w)}$, via $I_1 \sim I_y^{(w)}\rho_x$. Dividing the ionosphere into the "coherent" regions with sizes ρ_x and ρ_y as shown in Fig. 6.13, we obtain that the number of such "coherent" currents covering the area $dxdy$ is of the order of $dN \sim dxdy/\left(\rho_x\rho_y\right)$. Since these currents are

uncorrelated, the net amplitude of the magnetic variations is close to zero whereas the sum of squared amplitudes is proportional to dN; that is, the contribution of the area $dxdy$ is of the order of $d\left(\delta B_x\right)^2 = \delta B_{1x}^2 dN$. Combining above relationships with Eq. (6.100) and integrating gives the amplitude of the net squared magnetic variations

$$\delta B_x^2 = \frac{\mu_0^2 \left(I_y^{(w)}\right)^2 \rho_x \rho_y}{16\pi^2} \int\limits_{-\infty}^{\infty} \int\limits_{-\infty}^{\infty} \frac{dxdy}{\left(x^2 + y^2 + d^2\right)^3}. \tag{6.101}$$

Performing integration over x and y, taking into account that the power spectrum of the magnetic noise is proportional to δB_x^2, and replacing $\left(I_y^{(w)}\right)^2$ by the spectral density of random current fluctuation $\Theta(\omega)$, we obtain

$$\Psi_{xx}^{(B)}(\omega) = \frac{\mu_0^2 \rho_x(\omega)\, \rho_y(\omega)\, \Theta(\omega)}{32\pi d^2}. \tag{6.102}$$

This rough estimate coincides with Eq. (6.89) to an accuracy of the numerical factor $\pi/8$. This detailed calculation made in previous sections is totally consistent with the simple model presented above.

6.4.6 *Flicker-Noise of Ionospheric Currents*

The ionospheric currents and conductivity are subject to violent changes from the action of many forces: variations of the solar radiation, MHD waves and particle precipitation from the magnetosphere, fluctuations of the plasma number density, turbulence occurring in the plasma and neutral gas flows, and etc. A close analogy exists with conductivity of the electric devices, in which the low-frequency current fluctuations are supposed to be due to slow fluctuations of both the medium resistance and the source emissivity, which are in turn provided by a superposition of a great number of random processes with different relaxation times. This kind of electromagnetic noise is termed flicker-noise or $1/f$ noise since overall the power spectrum of this noise, $F(f)$, tends to decrease inversely proportional to the frequency, i.e.,

$$F(f) = K \frac{\langle J \rangle^m}{f^n}, \tag{6.103}$$

where $\langle J \rangle$ is the mean current density, K, m, and n are the empirical constants, and $f = \omega/(2\pi)$ is frequency. The exponent n in Eq. (6.103) varies within the interval $0.8 < n < 1.2$, but in most cases n is close to unity while $m \approx 2$ (Rytov et al. 1978; Weissman 1988). This universal dependence has been observed

in gas-discharge devices, electrolytes, granulated resistance, germanium and silicon diodes, photoelectric cells, contact resistances, thermistor, and etc. Surprisingly, our understanding of the flicker-noise is not so good as it should be, given its commonplace occurrence. This type of noise is supposed to be provided by a superposition of a large number of random processes with different relaxation times, including slow fluctuations of both the medium resistance and the source emissivity.

Here we assume the presence of the flicker-noise in the spectral density of the ionospheric wind-driven currents. In such a case the mean current density in Eq. (6.103) should be replaced by the mean height-integrated currents, $\left\langle I_l^{(w)} I_p^{(w)} \right\rangle^{1/2}$, in such a way that Eq. (6.103) is transformed to

$$F_{lp}(f) = K \frac{\left\langle I_l^{(w)} I_p^{(w)} \right\rangle^{m/2}}{f^n}, \tag{6.104}$$

Notice that if the currents $I_l^{(w)}$ and $I_p^{(w)}$ are uncorrelated, then the function $F_{lp}(f)$ vanishes.

Substituting Eq. (6.104) into Eq. (6.92) gives an order-of-magnitude estimate of power spectrum on the ground surface. For simplicity we choose the case $F_{xy} = F_{yx} = 0$ and $m = 2$ that gives

$$\Psi_{xx}^{(B)} = \frac{\mu_0^2 V_a^2 K}{256 d^2 f^{2+n}} \left\{ \left(\frac{3\alpha_H^2}{g_3} + g_3 \right) \left\langle I_x^{(w)} \right\rangle^2 + \left(\frac{\alpha_H^2}{g_3} + 3g_3 \right) \left\langle I_y^{(w)} \right\rangle^2 \right\} \tag{6.105}$$

where $\left\langle I^{(w)} \right\rangle$ stands for the mean amplitude of the height-integrated ionospheric current, which can be estimated as

$$\begin{aligned} \left\langle I_x^{(w)} \right\rangle &= B_0 \left(\Sigma_H \langle V_\perp \rangle - \Sigma_P \left\langle V_y \right\rangle \right) \sin\gamma, \\ \left\langle I_y^{(w)} \right\rangle &= B_0 \left(\Sigma_H \langle V_\perp \rangle + \Sigma_P \left\langle V_y \right\rangle \right), \end{aligned} \tag{6.106}$$

If the dispersion of the acoustic wave velocity is neglected, that is, V_a is a constant value, then the spectral density $\Psi_{xx}^{(B)}(f)$ is inversely proportional to f^{n+2}. Recently Surkov and Hayakawa (2007) have found that the presence of flicker noise in the atmospheric background current, can provide the same dependence of the ULF power spectrum on frequency.

To make a theoretical plot of the spectral amplitude we use the numerical values of the ionospheric and atmospheric parameters alluded to above. Taking the notice that $V_A = 5 \times 10^2$ km/s is best suited in the altitude range of the E layer, the ionospheric parameters $\alpha_P = 3.14$ and $\alpha_H = 4.71$ are chosen for the daytime ionosphere while $\alpha_P = 0.126$ and $\alpha_H = 0.188$ for the nighttime conditions. The mass velocity of the neutral gas in the ionosphere is estimated as $\left\langle V_y \right\rangle \sim \langle V_\perp \rangle \sim V_a \sim 10^2$ m/s and the angle of magnetic field inclination $\gamma = \pi/2$.

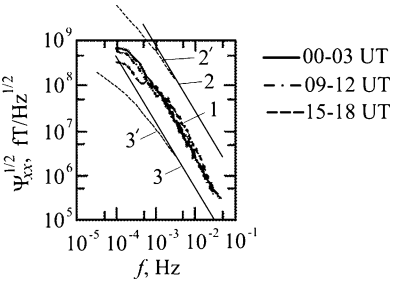

Fig. 6.14 Measured monthly average 3-h power spectra taken from Lanzerotti et al. (1990) (curve 1) and calculated power spectra of magnetic noise for the nighttime (2) and daytime (3) ionospheric parameters. The numerical calculations from improved equation (6.107) are shown with lines 2′ and 3′

The parameters appearing in empirical Eq. (6.103) is chosen as follows: $K = 1$ and $m = 2$. When Eq. (6.105) is compared with the evidence from ULF measurements (Lanzerotti et al. 1990), it is apparent that the spectral index $n = 1$ is a best fit value.

A model calculation of the square root of the spectral amplitude with a best fit value $n = 1$ and of the power spectrum recorded at Arrival Heights, Antarctica in June 1986 (Lanzerotti et al. 1990) are presented in Fig. 6.14 as a function of frequency f. The observational data taken from Lanzerotti et al. (1990) are shown with line 1 while our model calculations are plotted with line 2 (daytime conditions) and 3 (nighttime conditions). It is obvious from Fig. 6.14 that the observational data are sandwiched between the theoretical lines 1 and 2. It should be noted that there are some uncertainties in the ionospheric current parameters, for example, in the constant K in Eq. (6.104).

We recall that 1D distribution of the ionospheric wind-driven currents results in the 2D spectral amplitude in inverse proportion to the squared frequency, which in turn leads to a discrepancy between the predicted and measured spectra.

The observational data slightly deviate from the straight line as is seen in the upper corner of Fig. 6.14. In this frequency range the correlation radius may be greater than or equal to the distance between the Earth and the ionosphere. In such a case the approximate solution given by Eq. (6.89) should be replaced by the more accurate solution. To gain better understanding of this behavior of the observational data, consider the case $\rho_x = \rho_y = \rho_c(\omega)$. Substituting Eqs. (6.84), (6.87) into Eq. (6.81) and applying an inverse Bessel transform yields

$$\Psi_{xx}^{(B)}(\omega) = \frac{\mu_0^2 \Theta(\omega)}{32}\left[1 - \frac{2\pi^{1/2} d}{\rho_c(\omega)} \exp\left(\frac{4d^2}{\rho_c^2(\omega)}\right)\left\{1 - \operatorname{erf}\left(\frac{2d}{\rho_c(\omega)}\right)\right\}\right]. \tag{6.107}$$

Given the above parameters and based on Eq. (6.107), the numerical calculations are shown in Fig. 6.14 with lines 2′ and 3′. In the low-frequency limit, when $\rho_c(\omega) \gg 2d$, the expression in square bracket tends to unity whence it follows that $\Psi_{xx}^{(B)}(\omega) \propto \Theta(\omega) \propto \omega^{-1}$. This means that the spectral index of the power

spectrum must fall off with a decrease in frequency followed by the decrease in inclination angle of the lines $2'$ and $3'$ as shown in Fig. 6.14.

The lines 3 and $3'$, which correspond to the nighttime parameters of the ionosphere, lie below the experimental data. To explain this discrepancy with observations, one may assume the presence of supplementary sources, which contribute the ULF noise at nighttime.

6.4.7 Neutral Gas Turbulence

Turbulence of neutral gas flow in the altitude range of the E layer can serve as an alternative excitation source of the ULF electromagnetic noise. As we have noted above, if a neutral gas flow is stirred in some region with size λ, turbulization of flow may occur in a so-called inertial subrange, $\lambda^{-1} \ll k \ll \lambda^{-1}\mathrm{Re}^{3/4}$, in k space. It is usually the case that the Reynolds number, Re, tends to maximize in the vicinity of turbopause and it can be large enough in the E-layer, that is about 10^2–10^4 as it follows from the assessment we made in Sect. 5.3.6. The Kolmogorov spectrum covers the frequency range given by Eq. (5.72). Assuming for the moment that the smoothed mean mass velocity of the gas flow is $V = 10^2$ m/s, and the typical scale of the turbulization of flow is $\lambda = 10^2$ km we get the estimate $1.6 \times 10^{-4} \ll f \ll (0.005\text{–}0.16)$ Hz. According to the Kolmogorov theory for an isotropic homogeneous medium, in this frequency region the mechanical energy of the turbulent flow has a power law spectrum $\propto k^{-5/3}$.

The correlation matrix of the ionospheric wind-driven current can be expressed through the spectral density of the mass velocity fluctuations $\left\langle \delta V_l \delta V_p^* \right\rangle$ which in turn is proportional to the spectral density of the mechanical energy. Since the typical frequencies of turbulent pulsations are evaluated as $\omega \sim kV$, we can thus assume that the functions $F_{lp}(\omega) \propto \omega^{-5/3}$. Considering 2D distribution of the height-integrated currents in the ionosphere we come to the dependence $\Psi_{xx}^{(B)}(\omega) \propto \omega^{-11/3}$. The spectral index $11/3$ of the correlation function $\Psi_{xx}^{(B)}(\omega)$ slightly differs from the best fit value 3, which corresponds to the data shown in Fig. 6.14. The best hope for that is the case of 1D distribution of the wind-driven ionospheric currents when we obtain $\Psi_{xx}^{(B)}(\omega) \propto \omega^{-8/3}$.

6.4.8 Random Variations of Background Atmospheric Current and Conductivity

The mean value of the background atmospheric current density due to atmospheric conductivity is about $(3.5\text{–}4) \times 10^{-12}\,\mathrm{A/m^2}$. Recently Davydenko et al. (2004) have studied the electric environment of a mesoscale convective system (MCS). The typical size of the MCS-trailing stratiform region was estimated to be about

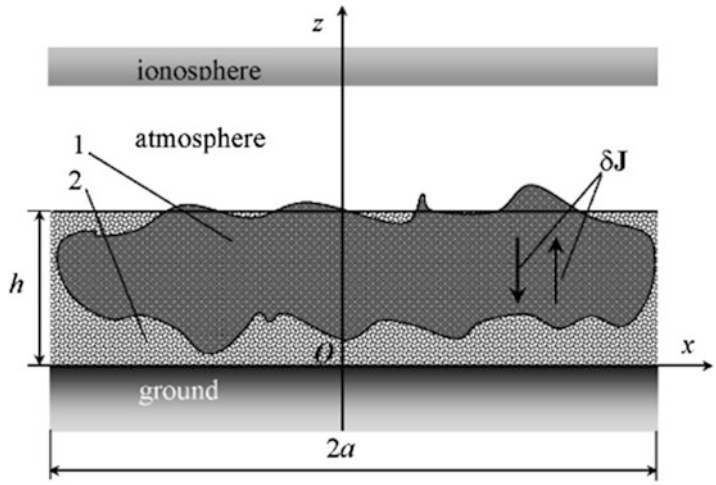

Fig. 6.15 A schematic drawing of current fluctuations in the vicinity of large-scale atmospheric inhomogeneities

200 km and the total vertical current in this region was 25 A, which is much greater than the contribution of an isolated thunderstorm ($\sim$ 0.4 A). In the region surrounding the thunderstorm, the atmospheric current density reached a peak value of about (3.5–1.2) $\times 10^{-9}$ A/m^2. Interestingly, both the atmospheric current in the MCS-trailing stratiform region and the mean current due to lightnings discharges were upward-directed. Considering the important role played by the atmospheric background current in formation of the global electric circuit, it is expected that the random current fluctuations may attribute to the electromagnetic noise.

In this notation the atmospheric current flowing in the vicinity of large-scale atmospheric inhomogeneities such as thunderstorms or hurricanes is treated as a stochastic process. We estimate the spectrum and amplitude of correlation function of the electromagnetic noise caused by the random current and conductivity fluctuations and discuss whether such a noise contributes to natural electromagnetic background in the range of 10^{-4}–10^{-2} Hz.

Following Surkov and Hayakawa (2007) we assume that the current variations are upward or downward inside the perturbed region and are zero outside, as shown in Fig. 6.15. To simplify the problem the actual inhomogeneous region labeled 1 is replaced by a cylindrical region with the radius a and the height h labeled 2. As before the random current fields are assumed to be steady, uniform, and isotropic inside the inhomogeneity, which, in turn, implies that the spectral density of the process is delta-correlated. To relate the electromagnetic spectra with current fields, a transfer matrix should be found, and then we can calculate the correlation matrix and power spectra of the random electromagnetic field.

In order to derive the main results we consider a simple way using the following line of reasoning. First, we note that the fluctuations of the atmospheric current

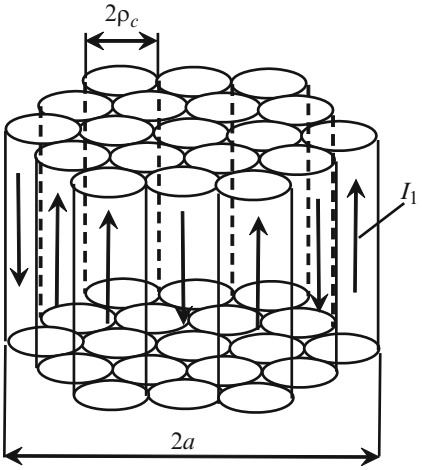

Fig. 6.16 A simplified model used to give simple interpretation and to indicate physical meaning of the results. The atmospheric current fluctuations are correlated inside each vertical cylinder but are not correlated with respect to each other

can be considered as the correlated current fluctuations inside the vertical cylinder with radius of the order of $\rho_c(\omega)$. The net current flowing through the cross-section of this cylinder is estimated as $I_1 = \pi\rho_c^2 \langle \delta J \rangle$, where $\langle \delta J \rangle$ is the mean amplitude of the current density fluctuations. In the first approximation we neglect the coupling due to the magnetic field generated by each current cylinder. Dividing the whole perturbed region into parts/cylinders with radii ρ_c, as shown in Fig. 6.16, we obtain that the number of such "coherent currents" is of the order of $N \sim a^2/\rho_c^2$. Since these currents are uncorrelated, the net amplitude of the electric current variations is proportional to the square root of the current number, that is $I = I_1 N^{1/2} = \pi a \rho_c \langle \delta J \rangle$. At far distances the magnetic field of the vertical current can be expressed through the current moment Ih. Assuming for the moment that the non-conductive atmosphere with thickness d is "sandwiched" between two conductive plates, which approximate the ionosphere and the ground, the solution of the problem is given by Eq. (4.40). Replacing the current moment $M(\omega)$ by the value Ih and taking into account that $\cot(\theta/2) \approx 2/\theta \approx 2R_e/r$ yields

$$\delta B_\phi = \frac{\mu_0 I h}{2\pi r d}, \tag{6.108}$$

where δB_ϕ denotes the azimuthal magnetic field and r is radial distance to the vertical current moment. If the exponential atmospheric conductivity [Eq. (3.1)] is allowed for, the parameter d in Eq. (6.10) should be replaced by the vertical scale, H, of the conductivity variations with height. Such a characteristic scale can serve as an effective thickness of "insulator" layer. Substituting I and H into Eq. (6.108), we obtain

$$\delta B_\phi = \frac{\mu_0 a \rho_c h}{2rH} \langle \delta J \rangle . \tag{6.109}$$

Taking into account that the power spectrum of the magnetic noise is proportional to δB_ϕ^2 and replacing $\langle \delta J \rangle^2$ by the spectral density of random current fluctuation $F(f)$ yields

$$\Psi^{(B)}(r, f) \sim \left(\frac{\mu_0 a \rho_c h}{2rH} \right)^2 F(f), \tag{6.110}$$

where $f = \omega/(2\pi)$.

The background atmospheric currents mainly depend on the air conductivity which, in turn, is subject to violent changes from the action of the winds, precipitations, air humidity, pressure and temperature and etc. Thus, there may be many causes of the background conductivity and current fluctuations. This means that there may be the same mechanisms, which lead to the flicker-noise spectral density. Substituting Eq. (6.103) for $F(\omega)$ and Eq. (6.91) for $\rho_c(f)$ into Eq. (6.110), we finally obtain the rough estimate of the power spectrum

$$\Psi^{(B)}(r, f) \sim \frac{K \langle \delta J \rangle^m}{f^{n+2}} \left(\frac{\mu_0 a V_a h}{2rH} \right)^2 . \tag{6.111}$$

When $h \ll H$, the above equation coincides with the result obtained by Surkov and Hayakawa (2007) to an accuracy of factor 2.

On the basis of the assumption that the ULF atmospheric background current fluctuations exhibit a power law noise with the spectral index n we have found that the power spectra of magnetic noise must vary on overall inversely proportional to f^{n+2}. It is interesting to note that if n is close to unity, then the magnetic noise power spectra vary as f^{-3}, which is totally compatible with the measured dependence in the frequency range of 5×10^{-4} to 5×10^{-2} Hz (Lanzerotti et al. 1990).

The theoretical line calculated from Eq. (6.111) approximately coincides with line 3 shown in Fig. 6.14 that is lower, but nearly parallel to the experimental data shown with line 1. It should be noted that we have considered only a single atmospheric inhomogeneity as the source of the electromagnetic noise. Meanwhile, the worldwide thunderstorms, whirlwinds, or hurricanes, which are in progress around the world at any time, may contribute to the net electromagnetic nose.

Before leaving this section, it should be noted that the ULF electric field noise in the atmosphere due to background current variations is estimated to be of the order of 20–0.7 μV/(m Hz$^{1/2}$) (Surkov and Hayakawa 2007). Such electric variations are practically undetectable since its amplitude lies below the actual electric noise level. This leads us to the conclusion that the atmospheric electric noise must arise due to another causes.

It should be emphasized that the mechanism we have treated above is not unique because other mechanisms of $1/f$ noise such as MHD waves and solar activity might also be operative.

6.4.9 Electric Field Pulsations at Fair-Weather Conditions

In this section we consider reasonably steady status of the Earth's electric field. This implies that no processes of charge separation are taking place in the atmosphere (Chalmers 1967). Here we focus our attention alone on short-term ULF electric field pulsations at fair-weather conditions in lower atmosphere. The study of the pulsations of both the atmospheric electric field and charge density is indicative of the existence of certain relation between these pulsations and the turbulent stirring of charged particles in surface air as well as the drift of space charge (e.g., see the papers by Ogden and Hutchinson 1970; Yerg and Johnson 1974; Anderson 1982; Hoppel et al. 1986; Anisimov et al. 1999). It is believed that the charge density behaves like a passive air-entraining admixture and the electric field spectra are therefore controlled by the neutral-gas turbulence that can drag the aero-electric structures in the near-surface atmospheric layer. In contrast to the traditional problem of the atmospheric turbulence which deals with the fluctuations of mass velocity and gas temperature, the electric field fluctuations are nonlocal values since they depend on the spatial distribution of atmospheric charges around observation point. Thus, the electric field and charge density pulsations in the lower atmosphere are a significant indicator of atmospheric dynamics at fair-weather conditions.

Anisimov et al. (2002) have reported that at the frequencies of 0.01–0.1 Hz the spectral density, $\psi^{(E)}$, of the electric field pulsations in the surface atmospheric layer obeys the power law $\psi^{(E)} \propto f^{-n}$. Under the fair-weather and fog conditions, the spectral index n varies in the range of 1.23–3.36 with the most probable value from 2.25 to 3.0. The study of the temporal variations has shown that the structured pulsations alternate with unstructured variations of the electric field. The spectral index of the structured pulsation lies within interval 2.03–3.36 whereas the spectra of the unstructured variations is characterized by $n = 1.23$–2.89. Furthermore, these latter variations have small amplitude and energy.

The structured pulsations are thought to be due to the aero-electric structures flying at a low altitude, which is of the order of the structure size. As would be expected, the main energy of the aero-electric pulsation is concentrated in the near-surface atmospheric layer. The theory predicts the spectral density of such electric variations to be $\psi^{(E)} \propto f^{-11/3}$.

The unstructured variations can be resulted from the distant submesoscale aero-electric structures, which move along with mean atmospheric air flow. If the turbulent pulsations in these structures lie in the inertial subrange, the Kolmogorov theory predicts that the power spectrum of the pulsations is proportional to $f^{-5/3}$. The spatial horizontal size of such structures is estimated as 0.5–1 km and their lifetime is not less than 10–20 min.

Under fog conditions the amplitude of electric pulsation was found to increase more than one order of magnitude whereas the spectral index of the fog aeroelectric field pulsations does not differ drastically from the fair-weather spectrum index (Anisimov et al. 2002).

6.4.10 Monitoring of Near-Earth Plasma

The measurements of the global electromagnetic resonances and ULF fields is extremely important in the study of both the magnetospheric plasma dynamics and the Earth's magnetosphere status as a whole. There exists a close analogy with seismology, in which seismic waves are used to study the Earth's interior structure. The fundamental difference between the two areas is that the position and spectrum of the seismic sources are usually known with assurance whereas we have only a rough measure of the source properties of the MHD waves incident to the ionosphere. The monitoring of near-earth plasma density and the study of the ionosphere conductivity have their basis in separating the resonance effects from the ULF natural and man-made noises. The idea of hydromagnetic diagnostics of the magnetosphere based on the resonance spectrum of a field line was originally suggested by Obayashi (1958) and Dungey (1963). The problem of the diagnostics can be split into two basic tasks; that is, the measurement of the FLR-frequencies and solution of the inverse problems to determine plasma parameters in the magnetosphere (Guglielmi 1974, 1989; Baransky et al. 1985, 1990). Plausibility of this technique is restricted by an instability of the solution of the inverse problem since this solution is rather sensitive to small perturbations of the initial data. In practice, such perturbations are present not only due to the measurement inaccuracy but also because of the variability of the magnetosphere itself.

Much progress toward better understanding of the global ULF electromagnetic resonances and noises has been achieved in the past decades, that results in the appearance of "hydromagnetic seismology" of the near-earth space.

6.4.11 Space Weather

Overall the space weather describes today's status of the space environment including the conditions on the Sun and in the solar wind, magnetosphere, ionosphere, and thermosphere. When the space environment is disturbed by the variable output of particles and radiation from the Sun, it can influence the performance and reliability of space-borne equipment including computer memories. The geomagnetic storms, substorms, cosmic and solar rays give rise to degradation of spacecraft material, primarily solar battery. The interrelation between the fluxes of high energy particles and onboard anomalies has been well documented. The failure quota due to

geophysical factors can reach about 60 % of total spacecraft failures (e.g., Pilipenko et al. 2006). Drastic deterioration of the space weather, that is fast increase in solar and geomagnetic activity, may greatly affect the ground-based technological systems and can endanger human life or health. At geostationary orbits the most dangerous effect is the influence of energetic particles on spacecraft performance. Depending on the particle energy, it can produce electrostatic charging followed by the faulty operation of electronics. The space-borne equipment errors have occurred during a magnetospheric storm just after a sharp enhancement of the relativistic electrons flux in the magnetosphere. The effect of these electrons is appearance of static negative charges, which can be irregularly distributed on the satellite surface because of different electric properties of surface elements. The potential drop between adjacent details of the satellite can reach tenth kilovolts that may result in dielectric breakdown and solar battery damage. Due to that the magnetospheric electrons with energy about 100 keV are termed "killer electrons." One of the best known events is a breakdown of American satellite TELSTAR during a magnetic storm in 1997, that resulted in the paging disconnection in considerable regions of the USA.

Sudden magnetospheric perturbations may greatly affect systems of communication and navigation including satellite navigation (GPS, GALLILEO and GLONASS) which in turn result in unforeseen contingencies (e.g., Yasuda et al. 2011; Takada et al. 2012). Air carriage comes up against such serious problems as a complete or particular loss of communication during the flight, delay of flight or changing of the flight routine, increase in fuel consumption, and fall off of gross weight. Moreover, the fluxes of high energy protons (with the energies greater than 100 MeV) of the solar flares can trigger health hazard for pilots and air travelers because of enhanced radiation background onboard. For example, the FAA (Federal Aviation Administration), which is primarily responsible for the safety and regulation of civil aviation in the USA, has reported that due to the strong solar flares on October 29 and 30, 2003 the global American system of precise GPS-positioning WAAS (Wide Area Augmentation System) was nonserviceable for aviation for 15 and 11 h, respectively. The intense radio bursts of clockwise-polarized waves in the frequency range of L1 and L2, which is usually used for satellite navigation, have been observed on December 2006. This results in the complete loss of GPS-signal for 10 min. With the current trend in miniaturization of electronic equipment, the impact of solar energetic particles greatly increases the risk of radiation damage of particular elements which may result in false operation and the generation of incorrect commands. For example, the failure probability of main memory module due to an impact of individual solar high energy particle was estimated to be one event per 200 h during the flight in polar region.

In the interest of air traffic, the space weather monitoring needs to include measurements of solar particle fluxes and Roentgen radiation, ejections of coronal plasma, and other characteristics of the solar activity provided by geostationary satellites as well as the observations of the particle flux variations in polar region and Earth radiation belts provided by polar satellites. Indices of solar and geomagnetic

activities, measurements of absorption in D region of the ionosphere and polar cap, and other ground-based observations provide us with additional information (Burov et al. 2013).

For monitoring and study of the space weather the modern geophysics has a powerful tool such as space stations between the Sun and the Earth, flotilla of satellites in near-earth orbits, solar radio-telescopes, a network of ground-based radars and magnetometers. One of the challenges of magnetospheric research is to know enough about the solar activity and geomagnetic storms to make it possible for us to forecast the space weather. Much emphasis has been put on studies of this problem during the last few decades due to the increasing deployment of radiation- current- and field-sensitive systems in space and complex technological systems on the Earth. Despite much success in the study of this problem, the space weather forecasting has not become purely an engineering problem and it remains a formidable task to be accomplished.

Appendix F: FLR Structure

In Sect. 6.2 we study the FLR theory on the basis of the "MHD box" model. The plasma dynamics is described by Eqs. (6.25)–(6.30) where all the perturbed quantities are assumed to vary as $\exp\left(-i\omega t + ik_y y\right)$. Eliminating the plasma velocity from this set of equations we are thus left with the set

$$i\omega E_x / V_A^2 = \partial_z \delta B_y - ik_y \delta B_z + \mu_0 J_x, \tag{6.112}$$

$$-i\omega E_y / V_A^2 = \partial_z \delta B_x - \partial_x \delta B_z - \mu_0 J_y, \tag{6.113}$$

$$\partial_z E_y = -i\omega \delta B_x, \tag{6.114}$$

$$\partial_z E_x = i\omega \delta B_y, \tag{6.115}$$

$$\partial_x E_y - ik_y E_x = i\omega \delta B_z. \tag{6.116}$$

Eliminating the variations of magnetic fields δB_x, δB_y, and δB_z from Eqs. (6.112)–(6.116) we come to the set

$$\left(\partial_z^2 + k_A^2\right) E_x = ik_y \left(\partial_x E_y - ik_y E_x\right) - i\mu_0 \omega J_x, \tag{6.117}$$

$$\left(\partial_x^2 + \partial_z^2 + k_A^2\right) E_y = ik_y \partial_x E_x - i\mu_0 \omega J_y, \tag{6.118}$$

where $k_A^2 = \omega^2 / V_A^2$. Notice that if $k_y = 0$, Eqs. (6.117) and (6.118) are similar to Eqs. (6.31) and (6.32). The boundary conditions at the "MHD box" sides, which correspond to the northern ($z = l_1$) and the southern ionospheres ($z = 0$), are given by Eq. (6.35)

Using a variable separation method, we seek for the solution of Eqs. (6.117) and (6.118) in terms of the series

$$E_x = \sum_n a_n(x)\, q_n(z) \quad \text{and} \quad E_y = \sum_n b_n(x)\, q_n(z), \tag{6.119}$$

where the eigenfunctions, $q_n(z)$, of the problem must satisfy the following equation

$$\frac{d^2 q_n}{dz^2} + k_n^2 q_n = 0, \tag{6.120}$$

where k_n denotes the eigenvalues of the problem. The solution of Eq. (6.120) is given by

$$q_n = C_1 \sin k_n z + C_2 \cos k_n z. \tag{6.121}$$

To find the undetermined constants C_1, C_2 and the eigenvalues, one should substitute Eq. (6.119) for E_x and E_y into boundary conditions (6.35) to yield

$$\frac{dq_n}{dz} = \pm i\omega\mu_0 \Sigma_P^{\pm} q_n. \tag{6.122}$$

Here the sign plus and Σ_P^+ correspond to the northern ionosphere, i.e., $z = l_1$, while the sign minus and Σ_P^- correspond to the southern ionosphere, i.e., $z = 0$. Substituting Eq. (6.121) for q_n into Eq. (6.122) and rearranging, we come to the set of algebraic equations for the constants C_1 and C_2. These equations have nontrivial solutions under the requirement that

$$\exp(-2ik_n l_1) = \frac{(1 - X_+)(1 - X_-)}{(1 + X_+)(1 + X_-)}, \tag{6.123}$$

where

$$X_{\pm} = \frac{\mu_0 \omega \Sigma_P^{\pm}}{k_n}. \tag{6.124}$$

Consider first two opposite extreme cases of zeroth and infinite Pedersen conductivities. If $\Sigma_P = 0$ at both the conjugate ionospheres, the right-hand side of Eq. (6.123) is equal to unity. The same is true in the inverse case of the perfectly conducting ionosphere when both $\Sigma_P^{\pm}$ and $X_{\pm}$ tend to infinity. In these extreme cases Eq. (6.123) has only real roots

$$k_n = \pi n / l_1, \tag{6.125}$$

where $n = 1, 2, 3 \ldots$ Moreover, these eigenvalues are independent of both the frequency ω and coordinate x.

In a general case of finite $\Sigma_P^{\pm}$ Eq. (6.123) has a discrete spectrum of complex eigenvalues k_n. The normalized eigenfunctions of the problem that obey Eqs. (6.120) and (6.122) can be written as

$$q_n = \frac{\sin k_n z}{k_n} + \frac{i \cos k_n z}{\mu_0 \omega \Sigma_P^-}. \tag{6.126}$$

First of all we note that these functions satisfy both Eq. (6.120) and the boundary condition (6.122) at $z = 0$. Moreover, substituting Eq. (6.126) for q_n into the boundary condition (6.122) at $z = l_1$ we come to the identity taking into account Eq. (6.123).

It can be shown that these eigenfunctions form a set of orthonormal functions in the sense that

$$\int_0^{l_1} q_n(z)\, q_m(z)\, dz = \delta_{nm}, \tag{6.127}$$

where δ_{nm} denotes the Kronecker symbol

$$\delta_{nm} = \begin{cases} 1, & n = m; \\ 0, & n \neq m. \end{cases} \tag{6.128}$$

To find the functions $a_n(x)$ and $b_n(x)$ we substitute Eq. (6.119) for E_x and E_y into Eqs. (6.117) and (6.118)

$$\sum_m \left(k_A^2 - k_m^2\right) a_m q_m = i k_y \sum_m \left(b_m' - i k_y a_m\right) q_m - i \mu_0 \omega J_x, \tag{6.129}$$

$$\sum_m \left\{b_m'' + \left(k_A^2 - k_m^2\right) b_m\right\} q_m = i k_y \sum_m a_m' q_m - i \mu_0 \omega J_y, \tag{6.130}$$

where the prime denotes derivative with respect to x.

Now we consider free oscillations of the electromagnetic field in the MHD box. In other words, the sources of the driving/external currents and perturbations are assumed to be "turn off" so that $J_x = J_y = 0$. Multiplying both sides of Eqs. (6.129) and (6.130) by $q_n(z)$, integrating these equations over z from 0 to l_1 and using the orthogonality condition (6.127) we are thus left with the set

$$i k_y b_n' = \left(k_A^2 - k_n^2 - k_y^2\right) a_n, \tag{6.131}$$

$$i k_y a_n' = b_n'' + \left(k_A^2 - k_n^2\right) b_n. \tag{6.132}$$

Eliminating a_n from Eqs. (6.131) and (6.132) and rearranging, we obtain

$$b_n'' - \frac{k_y^2 \left(k_A^2\right)' b_n'}{\left(k_A^2 - k_n^2\right)\left(k_A^2 - k_n^2 - k_y^2\right)} + \left(k_A^2 - k_n^2 - k_y^2\right) b_n = 0. \tag{6.133}$$

The solution of Eq. (6.133) depends on the boundary conditions at $x = 0$ and $x = l_2$. Without specifying these boundary conditions, we now will study the differential equation (6.133) to find some features which are common to all solutions. This equation exhibits strong singularities found in the denominator of its second term. Assuming for the moment that $k_A(x) = \omega / V_A(x)$ is a monotonic function of x, then Eq. (6.133) may have two regular singular points, say $x = \xi$, where

$$k_A^2(\xi) = k_n^2, \tag{6.134}$$

and $x = \eta$ where

$$k_A^2(\eta) = k_n^2 + k_y^2. \tag{6.135}$$

Following Southwood (1974), we suppose that the value of η in Eq. (6.135) is real and consider a small neighborhood of the singular point $x = \eta$ where the function k_A^2 can be expanded in a power series of $x - \eta$, that is, $k_A^2 \approx k_n^2 + k_y^2 + \left(k_A^2\right)'(x - \eta) + o(x - \eta)$. Here the derivative $\left(k_A^2\right)'$ is taken at $x = \eta$. In the first approximation Eq. (6.133) is thus reduced to

$$b_n'' - \frac{b_n'}{x - \eta} + \left(k_A^2\right)'(x - \eta)\, b_n = 0. \tag{6.136}$$

Southwood (1974) has shown that two independent solutions of Eq. (6.136) are finite at the singular point $x = \eta$. The implication of this singularity is that $x = \eta$ corresponds to a turning point, where the solutions change in character. We cannot come close to exploring this problem in any detail, but we need to note that this point divides a space of MHD box into two regions. In the first region the solutions are quasioscillatory in nature, whereas in the next one the solutions are monotonically increasing or decreasing functions of distance. In other words, the point $x = \eta$ corresponds to a turning point where solutions change from being oscillatory in nature to characteristically growing or decaying with coordinate x.

More importantly, the solution can be infinite at the next singular point, $x = \xi$, which corresponds to the FLR conditions. Indeed, substituting $k_n = k_A$ into Eqs. (6.123) and (6.124) we come to Eq. (6.37), which describes the resonance frequencies of the Alfvén oscillations. The implication here is that if $k_A^2(\xi) = k_n^2$ then the field line at $x = \xi$ will resonate with the shear Alfvén wave since the wave frequency ω equals to one of the Alfvén resonance frequencies.

If the energy dissipation in the conjugate ionospheres is neglected, the eigenvalues are given by $k_n = \pi n / l_1$, that is, they are real whence it follows that the resonant point ξ is real as well. In the dissipative case the parameter k_n^2 is a complex value so that the roots of Eq. (6.134) are in the complex plane x. Decomposing the roots x_n into its real and imaginary parts, we obtain $x_n = \xi_n + i\delta_n$. In what follows we do not specify the value and sign of δ_n.

Expanding k_A^2 in a power series of $x - (\xi_n + i\delta_n)$ we can reduce Eq. (6.133) to the form

$$b_n'' + \frac{b_n'}{x - \xi_n - i\delta_n} - k_y^2 b_n = 0. \tag{6.137}$$

The general solution of Eq. (6.137) is given by

$$b_n = AI_0(\tilde{x}) + BK_0(\tilde{x}), \tag{6.138}$$

where $\tilde{x} = k_y(x - \xi_n - i\delta_n)$ is a dimensionless variable, I_0 and K_0 are modified Bessel functions of order zero, and A and B denote arbitrary constants. We recall that this solution is valid only near the singular points $x_n = \xi_n + i\delta_n$.

It should be noted that the function K_0 has a logarithmic singularity in the neighborhood of zero point, i.e., $K_0(\tilde{x}) \propto -\ln\tilde{x}$ as $\tilde{x} \to 0$. This means that if the energy dissipation is negligible, that is to say $\delta_n = 0$, then the function K_0 is logarithmically infinite at $x = \xi_n$. Not surprisingly, the amplitude of the resonance may tend to infinity as the energy loss is ignored. Actually, the dissipation factor $\delta_n \neq 0$ so that for real x the solution (6.138) exhibits finite behavior near the point $x = \xi_n$. This notation has concerns with the electric field given by Eq. (6.119). In the vicinity of the resonant shell at $x = \xi_n$ we obtain the following asymptotic formula:

$$E_y \propto (\ln\tilde{x})\, q_n(z), \tag{6.139}$$

Substituting $k_A^2 = k_n^2$ into Eq. (6.131) gives $a_n = -ib_n'/k_y$ whence it follows that

$$E_x \propto q_n(z)/\tilde{x}. \tag{6.140}$$

Combining Eqs. (6.114) and (6.115) with Eqs. (6.139) and (6.140), we obtain

$$\delta B_x \propto \ln\tilde{x}\frac{dq_n(z)}{dz}, \tag{6.141}$$

$$\delta B_y \propto \frac{1}{\tilde{x}}\frac{dq_n(z)}{dz}. \tag{6.142}$$

In order to find δB_z one should use the series development of $K_0(\tilde{x})$ up to the terms $\sim \tilde{x}^2\ln\tilde{x}$. As a result we get

$$\delta B_z \propto \left(1 + \frac{\tilde{x}^2}{2}\ln\tilde{x}\right) q_n(z). \tag{6.143}$$

As is seen from the above equations, the field components E_x and δB_y, which contain the factor $\tilde{x}^{-1}$, reach a peak value near the point $x = \xi_n$ whereas the components E_y and δB_x have logarithmic, that is, weak singularities, and δB_z is a slowly varying function of $\tilde{x}$ in this region.

To study the shape of resonance components, E_x and δB_y, in a little more detail we use the representation of $\tilde{x}^{-1}$ in the form

$$\frac{1}{\tilde{x}} = \frac{\exp(i\varphi)}{\left\{(x-\xi_n)^2 + \delta_n^2\right\}^{1/2}}, \tag{6.144}$$

where the argument φ of complex number is determined via

$$\tan\varphi = \frac{\delta_n}{x-\xi_n}. \tag{6.145}$$

It is clear from Eq. (6.144) that near the resonant point the dependence $|E_x|^2$ and $\left|\delta B_y\right|^2$ on x has a form of Lorentz's curve outlined in Fig. 6.3. The normalized component $\left|\delta B_y\right|^2$ versus normalized variable x/ξ_n is sketched in this figure with solid line 1. The Lorentz's curve has a maximum at $x = \xi_n$ and the parameter $|\delta_n|$ is the characteristic half-width of this maximum. The argument/phase φ of E_x and δB_y changes by π when crossing the maximum. A schematic plot of the component δB_x is shown in Fig. 6.3 with dashed line 2.

In conclusion it should be noted that if $V_A(x)$ is not a monotonic function there may be more turning and resonance points.

References

Alperovich LS, Fedorov EN (2007) Hydromagnetic waves in the magnetosphere and the ionosphere. Springer, Berlin, 426 pp

Anderson RV (1982) The dependence of space charge spectra on Aitken nucleus concentrations. J Geophys Res 87:1216–1218

Anisimov SV, Mareev EA, Bakastov SS (1999) On the generation and evolution of aeroelectric structures in the surface layer. J Geophys Res D 104:14359–14367

Anisimov SV, Mareev EA, Shikhova NM, Dmitriev EM (2002) Universal spectra of electric field pulsations in the atmosphere. Geophys Res Lett 29(24):2217. doi:10.1029/2002GL015765

Annexstad JO, Wilson ChR (1968) Characteristics of Pg micropulsations at conjugate points. J Geophys Res 73:1805–1818

Atkinson G, Watanabe T (1966) Surface waves on the magnetospheric boundary as a possible origin of long period micropulsations. Earth Planet Sci Lett 1:89–91

Baransky LN, Borovkov YuE, Gokhberg MB, Krylov SM, Troitskaya VA (1985) High resolution method of direct measurement of the magnetic field lines eigenfrequencies. Planet Space Sci 33:1369–1374

Baransky LN, Belokris SP, Borovkov YuE, Green CA (1990) Two simple methods for the determination of the resonance frequencies of magnetic field lines. Planet Space Sci 38:1573–1576

Baumjohann W, Glassmeier KN (1984) The transient response mechanism and Pi2 pulsations at substorm onset: review and outlook. Planet Space Sci 32:1361–1370

Burov VA, Lapshin VB, Syroezhkin AV (2013) Space weather and air traffic. World of measurements (Mir Izmereniy), No. 2. pp 11–16 (in Russian)

Chalmers JA (1967) Atmospheric electricity, 2nd edn. Pergamon, New York

Chen L, Hasegawa A (1974) Plasma heating by spatial resonance of Alfvén wave. Phys. Fluids 17:1399

Cornwall JM (1965) Cyclotron instabilities and electromagnetic emission in the ultra low frequency ranges. J Geophys Res 70:61–69

Crowley G, Hughes WJ, Jones TB (1987) Observational evidence of cavity modes in the Earth's magnetosphere. J Geophys Res 92:12233–12240

Cummings WD, O'Sullivan RJ, Coleman PJ Jr (1969) Standing Alfvén waves in the magnetosphere. J Geophys Res 74:778–793

Davydenko SS, Mareev EA, Marshall TC, Stolzenburg M (2004) On the calculation of electric fields and currents of mesoscale convective systems. J Geophys Res 109:D11103. doi:10.1029/2003JD003832

Dowden RL (1966) Micropulsation "nose whistlers". A helium explanation. Planet Space Sci 14:1273–1274

Dungey JW (1954) Electrodynamics of the outer atmospheres. Ionosphere Scientific Report, vol 69. Ionosphere Research Labaratory, Cambridge

Dungey JW (1963) The structure of the exosphere, or, adventures in velocity in geophysics. In: DeWitt C, Hieblot J, Lebeau A (eds) The earth's environment proceedings of the 1962 Les Houches Summer School. Gordon and Breach, New York, pp 503–550

Engebretson MJ, Zanetti LJ, Potemra TA (1986) Harmonically structured ULF pulsations observed by the AMPTE/CCE magnetic field experiment. Geophys Res Lett 13:905–908

Engebretson MJ, Zanetti LJ, Potemra TA, Baumjohann W, Lühr H, Acua MN (1987) Simultaneous observation of Pc3–4 pulsations in the solar wind and the Earth's magnetosphere. J Geophys Res 92:10053–10062

Fraser-Smith AC (1995) Low-frequency radio noise. In: Volland H (ed) Handbook of atmospheric electrodynamics, vol 1. CRC Press, Boca Raton, pp 297–310

Ginzburg VL (1970) The propagation of electromagnetic waves in plasmas. Pergamon Press, Oxford

Glassmeier K-H (1980) Magnetometer array observations of a giant pulsation event. J Geophys 48:127–138

Glassmeier K-H (1995) ULF pulsations. In: Volland H (ed) Handbook of atmospheric electrodynamics, vol 2. CRC Press, Boca Raton, pp 463–502

Guglielmi AV (1974) Diagnostics of the magnetosphere and interplanetary medium by means of pulsations. Space Sci Rev 16:331

Guglielmi AV (1989) Diagnostics of the plasma in the magnetosphere by means of measurement of the spectrum of Alfvén oscillations. Planet Space Sci 37:1011–1012

Guglielmi AV, Troitskaya VA (1973) Geomagnetic pulsations and diagnostics of the magnetosphere. Nauka, Moscow (in Russian)

Higbie PR, Baker DN, Zwicki RD, Belian RD, Asbridge JR, Fennell JF, Wilken B, Arthur CW (1982) The global Pc5 events of November 14–15. J Geophys Res 87:2337–2345

Hoppel WA, Anderson RV, Willet JC (1986) In earth's electrical environment. National Academic Press, Washington, DC, pp 149–165

Jacobs JA (1970) Geomagnetic micropulsations. Springer, Berlin

Junginger H, Geiger G, Haerendel G, Melzner F, Amata E, Higel B (1984) A statistical study of dayside magnetospheric field fluctuations with periods between 150 and 600 s. J Geophys Res 89:10757–10762

Karpman VI, Meerson BI, Mikhailovsky AB, Pokhotelov OA (1977) The effects of bounce resonance on wave rates in the magnetosphere. Planet Space Sci 25:573–585

Kato Y (1962) Geomagnetic pulsations and hydromagnetic oscillations of exosphere. J Phys Soc Jpn 17:71

Kivelson MG, Southwood DJ (1985) Resonant ULF waves: a new interpretation. Geophys Res Lett 12:49–52

Kivelson MG, Etcheto J, Trotignon JG (1984) Global compressional oscillations of the terrestrial magnetosphere: the evidence and a model. J Geophys Res 89:9851–9856

Krylov AL, Fedorov EN (1976) Concerning eigen oscillations of bounded volume of a cold magnetized plasma. Rep USSR Acad Sci (Dokl Akad Nauk SSSR) 231:68–70
Krylov AL, Lifshitz AF (1984) Quasi-Alfvén oscillations of magnetic surfaces. Planet Space Sci 32:481–489
Kwok YC, Lee LC (1984) Transmission of magnetohydrodynamic waves through the rotational discontinuity of Earth's magnetopause. J Geophys Res 89:10697–10708
Landau LD, Lifshitz EM (1982) Electrodynamics of continuous media, 2nd edn. Nauka, Moscow (in Russian)
Lanzerotti LJ (1978) Studies of geomagnetic pulsations. In: Lanzerotti LJ, Park CG (eds) Upper atmosphere research in Antarctica. American Geophysical Union as part of the Antarctic Research Series, vol 29, pp 130–156. doi:10.1029/AR029
Lanzerotti LJ, Fukunishi H (1974) Modes of MHD waves in the magnetosphere. Rev Geophys Space Phys 12:724–729
Lanzerotti LJ, Maclennan CG, Fraser-Smith AC (1990) Background magnetic spectra: $\sim 10^{-5}$ to 10^5 Hz. Geophys Res Lett 17:1593–1596
Lee D-L, Lysak RL (1989) Magnetospheric ULF waves coupling in the dipole model: the impulsive excitation. J Geophys Res 94:17097–17103
Lee D-L, Lysak RL (1990) Effects of azimuthal asymmetry on ULF waves in the dipole magnetosphere. Geophys Res Lett 17:53–56
Leonovich AS (2000) Magnetospheric MHD response to a localized disturbance in the ionosphere. J Geophys Res 105:2507–2519
Leonovich AS, Mazur VA (1993) A theory of transverse small-scale standing Alfvén waves in an axially symmetric magnetosphere. Planet Space Sci 41:697–717
McHenry MA, Clauer CR (1987) Modelled ground magnetic signatures of flux transfer events. J Geophys Res 92:11231–11240
Nishida A (1978) Geomagnetic diagnostics of the magnetosphere. Springer, New York
Obayashi T (1958) Geomagnetic pulsations and the Earth's outer atmosphere. Ann Geophys 14:464–474
Ogden TL, Hutchinson WCA (1970) Electric space-charge pulses near the ground in sunny weather. J Atmos Terr Phys 32:1131–1138
Ohl AI (1962) Pulsations during sudden commencements of magnetic storms and long period pulsations in high latitudes. J Phys Soc Jpn 17(supp. A-2, paper II-1B-3):24–26
Ohl AI (1963) Long period pulsations of the geomagnetic field. Geomagn Aeron 3:113–120
Pilipenko V, Vellante M, Fedorov E (2000) Distortion of the ULF wave spatial structure upon transmission through the ionosphere. J Geophys Res A105:21225–21236
Pilipenko V, Yagova N, Romanova N, Allen J (2006) Statistical relationship between satellite anomalies at geostationary orbit and high-energy particles. Adv Space Res 37:1192–1205
Radoski HR (1966) Magnetic toroidal resonances and vibrating field lines. J Geophys Res 71:1891–1893
Radoski HR (1967a) Highly asymmetric MHD resonances: the guided poloidal mode. J Geophys Res 72:4026–4033
Radoski HR (1967b) A note on oscillating field lines. J Geophys Res 72:418–419
Radoski HR, Carovillano RR (1969) Axisymmetric plasmaspheric resonances: toroidal mode. Phys Fluids 9:285–291
Rytov SM, Kravtsov YaA, Tatarsky VI (1978) Introduction to statistical radiophysics, P. 2, random fields. Nauka, Moscow (in Russian)
Samson JC, Jacobs JA, Rostoker G (1971) Latitude-dependent characteristics of long-period geomagnetic micropulsations. J Geophys Res 76:3675–3683
Sato T (1978) A theory of quiet auroral arcs. J Geophys Res 83:1042–1048
Singer HJ, Kivelson MG (1979) The latitude structure of Pc5 waves in space: magnetic and electric field observations. J Geophys Res 84:7213–7222
Singer HJ, Russell CT, Kivelson MG, Fritz TA, Lennartsson W (1979) Satellite observations of the spatial extent and structure of Pc3, 4, 5 pulsation near the magnetospheric equator. Geophys Res Lett 6:889–892

Southwood DJ (1974) Some features of field line resonances in the magnetosphere. Planet Space Sci 22(3):483–491

Southwood DJ (1980) Low frequency pulsation generation by energetic particles. J Geomagn Geoelectr 32(Suppl. II):75–88

Southwood DJ, Kivelson MG (1982) Charged particle behaviour in low-frequency geomagnetic pulsations, 2. Graphical approach. J Geophys Res Space Phys 87(A3):1707–1710

Surkov VV, Hayakawa M (2007) ULF electromagnetic noise due to random variations of background atmospheric current and conductivity. J Geophys Res 112:D11116. doi:10.1029/2006JD007788

Surkov VV, Hayakawa M (2008) Natural electromagnetic ULF noise due to fluctuations of ionospheric currents. J Geophys Res Space Phys 113:A11310. doi:10.1029/2008JA013196

Takada M, Nunomiya T, Ishikara T, Nakamura T, Levis BJ, Bennett LJ, Getley IL, Bennett BH (2012) Measuring cosmic-ray exposure in aircraft using real-time personal dosimeters. Radiat Prot Dosim 149(2):169–176

Takahashi K (1988) Multisatellite studies of ULF waves. Adv Space Res 8(9–10), 427–436

Takahashi KT, McPherron RL, Terasawa T (1984) Dependence of the spectrum of Pc3–4 pulsations on the interplanetary magnetic field. J Geophys Res 89:2770–2780

Trakhtengerts VY, Rycroft MJ (2008) Whistler and Alfvén mode cyclotron masers in space. Cambridge University Press, Cambridge, 354 p

Voelker H (1962) Zur Breitenabhä ngigkeit der Perioden erdmagnetischer Pulsationen. Naturwissenschaften 49:8–9

Weissman MB (1988) $1/f$ noise and other slow, nonexponential kinetics in condensed matter. Rev Mod Phys. 60:537–571

Yasuda H, Lee J, Yajima K, Hwang JA, Sakai K (2011) Measurement of cosmic-ray neutron dose onboard a polar route flight from New York to Seoul. Radiat Prot Dosimetry 146(1–3):213–216

Yerg DG, Johnson KR (1974) Short period fluctuations in the fair-weather electric field. J Geophys Res 79:2177–2184

Yumoto K (1984) Long-period magnetic pulsations generated in the magnetospheric boundary layer. Planet Space Sci 32:1205–1218

Zibyn KYu (1965) Properties and nature of geomagnetic pulsations with periods from 10 s to several minutes. Geomagn Aeron 5:494

Ziesolleck CWS, Menk FW, Fraser BJ, Webb PW (1993) Spatial characteristics of low Pc3-4 geomagnetic pulsations. J Geophys Res 98:197–207